Shock wave propagation in layered planetary interiors: Revisited

Julien Monteux, J. Arkani-Hamed

Shock Wave Propagation in Layered Planetary Interiors: Revisited

J. Monteux

Université Clermont Auvergne, CNRS, IRD, OPGC, Laboratoire Magmas et Volcans, F-63000 Clermont-Ferrand, France

J. Arkani-Hamed

Department of Physics, University of Toronto, Toronto, Canada

Department of Earth and Planetary Sciences, McGill University, Montreal, Canada

Abstract.

While major impacts during late accretion of a Mars type planet occur on a differentiated body, the characteristics of the shockwave propagation are poorly known within these layered objects. Here, we use iSALE-2D hydrocode simulations to calculate shock pressure in a differentiated Mars type body for impact velocities ranging from 5 to 20 km/s, impactor radii ranging from 50 to 200 km, and different rheologies. To better represent the distribution of shock pressure as a function of distance from the impact site at the surface, we propose two distinct regions in the mantle: a near field region that extends to 7-15 times the projectile radius into the target, where the peak shock pressure decays exponentially with increasing the distance from the impact site, and a far field region where the pressure decays strongly with the distance following a power law. At the core-mantle boundary, the peak shock pressure increases from the mantle side to the core side. The refracted shockwave travels within the core where the shock pressure decreases following a second power law. In this study, we fit the output obtained from iSALE hydrocode simulations to determine scaling laws that illustrate the influence of the distance from the impact site, the ray angle, the target rheology, the impactor size and the impact velocity. Finally we combine these shock-pressure scaling laws with the formalism proposed by Watters et al. [2009] to determine the impact heating induced by large impacts within a differentiated Mars.

1. Introduction:

Terrestrial planets are formed by accreting a huge number of planetesimals in the solar nebula [e.g., Chambers and Wetherill, 1998; Kokubo and Ida, 2000; Rafikov, 2003; Chambers, 2004; Raymond, et al., 2006]. The ultimate goal is to investigate the thermal evolution of a growing terrestrial planet while taking into account the impact heating, heating by short-lived and long-lived radioactive elements, and by the core formation process. Because partial melting and core formation occur when a protoplanet's radius exceeds ~2700 km [e.g., Senshu et al., 2002], about 47% of Mars' and 90% of the Earth's and Venus' masses are expected to be accreted in the presence of a liquid core. To estimate the thermal state of a growing planet it is necessary to determine the impact heating of its solid mantle and liquid core by each impactor.

The impact-induced shock pressure and temperature increase inside a planet has been investigated using elaborated numerical models developed to better understand shock physics [e.g., Ahrens and O'Keefe, 1987; Pierazzo et al., 1997; Mitani, 2003; Wuennemann et al., 2006; Wünneman et al., 2008; Ivanov et al., 2010; Bar and Citron, 2011; Kraus et al., 2011; Bierhaus et al., 2012; Stewart, 2011]. However, the numerical solutions demand considerable computer capacity and time and are not practical for investigating a huge number of impacts that occur during the growth of a planet. For example, the formation of a planet like Mars requires about $3x10^5$ planetesimals of ~100 km in diameter. On the other hand, the scaling laws derived on the basis of numerical solutions of the shock dynamic equations [e.g., Ahrens and O'Keefe, 1987; Pierazzo et al., 1997; Mitani, 2003; Monteux and Arkani-Hamed, 2016] require remarkably less computer power and time, and have been used by many investigators [e.g., Tonks and Melosh, 1992, 1993; Watters et al, 2009; Roberts et al., 2009; Arkani-Hamed and Olson, 2010a, 2010b; Ghods and Arkani-Hamed, 2011], mainly because of their simplicity and partly because the difference between their results and those obtained by the numerical simulations of the shock dynamic equations is likely within the tolerance of the errors introduced due to the uncertainty of pertinent physical parameters. We note that the existing scaling laws are applicable for uniform mantle models of terrestrial planets and cannot be used for planets consisting of a solid silicate mantle and a liquid iron core with drastically different physical properties. Extra formulations are required to relate the shock pressure and particle velocity at the base of the mantle to those at

the top of the core. Arkani-Hamed and Ivanov [2014] derived the required boundary conditions at the core-mantle boundary (CMB) of a Mars type planet for a vertical impact on the basis of Hugoniot equations, the equality of the reflected and the refracted shock pressures, the continuity of the vertical component of particle velocity, and the Snell's law relating the incident angle to the refracted angle of a shock ray at the boundary. This resulted in a set of coupled 8 trigonometric equations to be solved simultaneously for each shock ray. At each point of the core mantle boundary, with spacing of 1 degree colatitude, the equations were solved iteratively until the difference between the two successive solutions were within a set error limit. Although such a simulation is much faster than the corresponding hydrocode simulation, it still takes considerable time to determine impact heating in a growing planet that requires several hundred thousand impacts during the accretion. Recently, Monteux and Arkani-Hamed [2016] derived scaling laws in the mantle of a Mars size planet on the basis of systematic hydrocode modeling, using impact velocities ranging from 4 to 10 km/s for impactor sizes ranging from 50 to 200 km in radius, and two different mantle rocks of dunite and peridotite overlying the iron core. The ANEOS type equations of state were used for the dunitic mantle rocks and the iron core.

In the present study, we adopt a new technique based on hydrocode models by Monteux and Arkani-Hamed [2016] while deriving a new scaling law for the iron core to assess shock pressure and the shock-related temperature increase in the entire Mars type planet. A given shock front propagates from the impact site at the surface of the planet down to the CMB. It then partly reflects back to the mantle, and partly enters the core and continues propagating until it impinges the CMB in the antipodal hemisphere, where it partly enters the antipodal mantle and partly reflects and propagates in the antipodal core. The second section characterizes the shockwave propagation within a differentiated Mars size planet for different sets of parameters (impactor radius, impact velocity, and mantle rheology). The third section compares the results from the scaling laws with those obtained using hydrocode simulations. In the fourth section, impact-heated models determined on the basis of the scaling laws to demonstrate the feasibility of the models derived by the scaling laws. Discussions and concluding remarks are relegated to the fifth, final section.

2. Shockwave Propagation Inside A Mars-Type Planet:

Figure 1 shows the 2D axi-symmetric total pressure (shock + lithostatic) distribution inside a Mars size body of radius 3400 km with a core radius of 1700 km, created by an impactor of 200 km in radius and at an impact velocity of 10 km/s obtained by hydrocode simulation. The shock pressure produced near the surface decays as the shock wave propagates downward until the wave impinges the CMB, where it partitions into two waves, a reflected wave that propagates outward in the mantle, and a refracted wave that enters the core and propagates downward. The reflected wave arriving at a given point in the mantle travels much longer, hence is always weaker than the direct wave that propagates directly from the impact site to that point. The peak pressure at the point is produced by the direct wave. The effects of the two reflected waves, one at the surface and the other at the CMB are not considered on the temperature of the mantle in this study (see below). An abrupt pressure jump is created at the top of the core by the refracted wave. The pressure then continues decreasing while the wave propagates in the core.

A total of 11 hydrocode models were simulated by Monteux and Arkani-Hamed [2016] that included impact velocities of 4 to 10 km/s at increments of 1 km/s for an impactor of 50 km in radius, and the impactor radii of 50 to 200 km at increments of 50 km for an impact velocity of 10 km/s. Two mantle rock types of dunite and peridotite were considered for a Mars-type planet. The authors considered shock wave propagation in the mantle of the impacted hemisphere. Here we extend the models allowing the wave enter the core, hence providing a means to estimate the characteristics of shock pressure and the related temperature increase throughout the mantle and the core.

2.1 The Model Set Up

At the end of the planetary accretion, large impacts between planetesimals and protoplanets are frequent. The amount of energy dissipated during this regime of planetary evolution is large enough to significantly melt the growing planets and efficiently separate the metal phase from the silicate phase, resulting in the core formation. We consider a large impact between an

undifferentiated bolide and a differentiated Mars size planet using numerical hydrocode simulations.

a) Physical model

We investigate the shock pressure inside a Mars size model planet for impact velocities V_{imp} of 5 to 20 km/s and impactors radii R_{imp} of 50 to 200 km. Such impactors are likely to create large impact basins with sizes comparable to the giant impact basins of Mars that were formed between 4.3 and 4 Ga [Frey, 2008; Robbins et al., 2013]. The impactors are large enough to have important consequences on their target. However the impactors might be too small to have experienced a complete melting and full metal/silicate separation before the impact unless they formed during the early Solar System evolution [Ricard et al., 2017] Impacts involving differentiated impactors will lead to the fragmentation of the impactor's core before sinking through the target's mantle [Kendall and Melosh, 2016]. In our models, an impactor is simplified by a spherical body of radius R_{imp} with uniform dunitic composition. Since we do not consider a realistic impactor with a metallic core, we underestimate the actual impactor mass and, as a consequence, the kinetic energy available for impact heating. In our models, the impactor and the impacted mantle have the same properties (composition, strength, rheology, and equation of state).

The ultimate goal is to determine the impact heating during the accretion of terrestrial planets such as Mars and the Earth. The huge number of impacts during accretion makes it impractical to consider oblique impacts for two main reasons: it requires formidable computer time, but more importantly because of the lack of information about the impact direction, i.e. the impact angle relative to vertical and azimuth relative to north. The peak shock pressure produced along the vertical direction beneath the impact site by an oblique impact appears to depend approximately on the sine of the impact angle relative to horizon (see Figure 3 of Pierazzo and Melosh, 2000). This implies a shock pressure reduction by a factor of ~0.71 for the most probable impact angle of 45^{o} [Shoemaker, 1962] compared to that of a vertical impact, assuming that all other parameters are equal. For example an oblique impact velocity of about 15 km/s produces almost the same shock pressures as that produced by a vertical impact velocity of about

11 km/s. The difference between these two velocities is well within the variations of the impact velocities of the N-body accretion models of terrestrial planets [e.g., Agnor et al., 1999; Chambers, 2013]. Studies of more realistic accretion scenarios, which take into account the oblique impacts and allow escape of material, conclude that the final state of an accreted body is less sensitive to the details of the collision [Agnor and Asphaug, 2004; Kokubo and Genda, 2010]. Therefore, we consider only head-on collisions (vertical impacts) to model the thermo-mechanical evolution during an impact between a differentiated Mars size body and a large uniform impactor.

As emphasized by Monteux and Arkani-Hamed [2016], the rheology of the impacted body plays a key role on the propagation of the shockwave and on the subsequent impact heating. However, the rheology of protoplanets is difficult to constrain precisely and is strongly governed by its thermal evolution. Depending on its accretion rate, on its composition in radiogenic elements and on the occurrence of large to giant impacts, growing Mars-sized protoplanets likely consist of a partially to fully molten mantle overlying a liquid metallic core [Kaula, 1979; Solomatov 2000; Senshu et al., 2002; Ricard et al., 2009]. In the following study we consider that the rheology of the impacted protoplanets ranges between a "hydrodynamic model" with no-strength where both the dunitic mantle and the metallic core are inviscid materials, and a "model with strength" where the metallic core is an inviscid fluid while the dunitic mantle is treated using a pressure-, temperature-, and damage- dependent strength model.

Damage describes the transition from intact to fractured strength. Under a constant pressure, damage begins to accumulate when the material begins to flow plastically. Damage is maximum when the material is completely fractured. Among the damage models available in iSALE, we adopt the Ivanov damage model [Ivanov et al., 1997], which prescribes damage as a function of plastic strain. In this model the plastic strain at failure is an increasing function of the total pressure P (lithostatic pressure plus the shock-induced pressure). This model allows rapid brittle failure in tensile and low-pressure modes, and semi-brittle failure at high pressures. The damage model from Ivanov et al., [1997] is simpler than the model developed by Collins et al., [2004] where the plastic strain at failure is a function of the brittle-ductile and brittle-plastic transition pressures, both these parameters being poorly constrained in the early protoplanets context.

The thermal softening is an efficient process for large-scale events [Potter et al., 2012]. Depending on the temperature and more specifically on the melt fraction, the impacted material can behave as a solid material or as fluid. The transition from solid-like to fluid-like behavior occurs at a critical melt fraction of ≈40% for early mantle material (Solomatov, 2000). As it depends on the temperature, the thermal softening process also strongly depends on the pre-impact temperature that is unfortunately poorly constrained in the Martian case. In our iSALE models, we use the Ohnaka thermal softening model where the shear strength of rocks depends on temperature, and reduces to zero at the melting temperature.

In the "model with strength", we approximate the thermodynamic response of both the iron and dunitic material using the ANEOS equation of state [Thompson and Lauson, 1972, Benz et al., 1989]. To make our models as simple as possible we do not consider here the effects of porosity or low density weakening which are likely to be negligible in the deep interior of a planet. However, as a first step towards more realistic models, we investigate the influence of acoustic fluidization, thermal softening and damage. The simulation parameters are listed in Table 1.

b) Numerical model

We use the iSALE-2D axisymmetric hydrocode, which is a multi-rheology, multi-material hydrocode, specifically developed to model impact crater formation on a planetary scale [Amsden et al., 1980, Collins et al., 2004, Davison et al., 2010]. To enable a comparison of our models, for all our simulations, we use a 2 km grid resolution computational domain. The horizontal and vertical number of cells per projectile radius (*cppr*) is maintained constant within the impacted mantle (=1700) and within the impacted core (=850) (see Table 2). The number of *cppr* varies only within the impactor when varying the impactor radius (*cppr*=25 for R_{imp}=50km and *cppr*=100 for R_{imp}=100km). Such spatial resolutions should lead to an underestimation of the peak shock pressure ranging between 5% (close to the impact site) and 10% (far from the impact site) according to resolution studies [e.g., Pierazzo et al., 2008; Wünneman et al., 2008, Monteux and Arkani-Hamed, 2016].

iSALE requires the length of each time step (dt) and the maximum time step (dt_{max}). iSALE limits the time step by the speed of sound according to the Courant–Friedrichs–Lewy (CFL) condition while dt_{max} limits a timestep if it is smaller than the CFL-limited timestep. In our models, we use a dt_{max} value of 0.05 s. The minimum post impact monitoring time is set to the time needed by the shockwave to travel from the impact site through the entire core of the impacted planet.

In our iSALE models, we investigate the effects of the ray angle β relative to the symmetric axis (Figure 2). To compare the shock wave propagation along each path illustrated in Figure 2, we developed a numerical method to extract the shock pressure and temperature at a fixed position from all our simulations. As a consequence, instead of using tracers, the impact-induced pressure and temperature fields are extracted from a cell-centered Eulerian grid points [Monteux and Arkani-Hamed, 2016]. Hence, the distance D corresponds to the straight-line distance between the impact site and the grid point where the peak pressure is located. It approximates the distance along a shock ray (see the Discussion section). Hence, we refer to the straight line as the ray from now on. We also investigate the effects of the angle β of the straight line, i.e., the so called ray, relative to the symmetric axis (Figure 2). We emphasize that a ray does not enter the core when the ray angle β is larger than 30° in our model planet.

2.2 *The Reference Models*

Figure 3 (left) shows the peak shock pressure distribution along the axis of symmetry (β=0°) in a model with R_{imp}=50 km and V_{imp}=10 km/s. From Figure 3, we can identify 2 zones of particular interest: Zone 1 where the peak shock pressure P_{Z1} decreases exponentially with the distance from the impact site, and Zone 2 where the peak shock pressure P_{Z2} still decreases significantly though less rapidly with the distance. As we will see later, these 2 zones are particularly distinguishable for small values of R_{imp}. Considering V_{imp}=10 km/s is the average asteroid impact velocity on Mars [Bottke et al. 1994], we will define the case with R_{imp}=50 km and V_{imp}=10 km/s as our reference model. Figure 3 (right) illustrates that considering a differentiated impactor (with a dunitic mantle and a liquid iron core) slightly increases the peak shock pressure magnitude during the propagation of the shockwave within the impacted planet because of the

246 different mass repartition in the impactor. However, considering a differentiated impactor affects
247 neither the pressure decay in 2 zones nor the position of the limit between the two zones.
248
249 The shock wave generated by an impactor propagates toward the center of the planet, while the
250 shock pressure decays as the wave deposits energy in the form of irreversible work into the target
251 [Ahrens and O'Keefe, 1987]. Hence, the ability of the impacted material to deform when
252 experiencing large shock pressure is of the first importance for the characterization of the peak
253 shock pressure evolution. Figure 3 illustrates the influence of the mantle rheology on the shock
254 wave propagation. The peak shock pressure experienced within the mantle decreases more
255 rapidly in the model with strength than in the hydrodynamic model. In our models, the acoustic
256 fluidization and the damage play minor roles on the shockwave propagation compared to that of
257 the strength, because the lithostatic pressure is too high to allow fracturing of rocks.
258
259 If strength is present, shock waves attenuate faster because the rarefaction waves travel faster in
260 material with strength and, therefore, cause a more rapid decay behavior [Curran et al., 1977,
261 Bierhaus et al, 2013]. We note that the speed of sound in a strength-less material is given by
262 $c = \sqrt{K/\rho}$ where K is the bulk modulus and ρ the density. If the material has some strength, the
263 longitudinal wave speed is determined by $c_L = \sqrt{(K + 4/3\mu)/\rho}$ where μ is the shear modulus.
264 Because $c_L > c$, the speed of the first, direct wave is larger when the strength is accounted for
265 than in the hydrodynamic case, hence the shock waves attenuate faster in the models with
266 strength [Curran et al., 1977, Bierhaus et al, 2013]. Ultimately, if the speed of the rarefaction
267 wave depends on strength, then differences in strength should result in different attenuation
268 behaviors. However this point is beyond the scope of our study. Outside Zone 1, the peak shock
269 pressure continues to decrease with distance from the impact site and both models show a similar
270 behavior: a power-law decrease followed by a pressure jump at the CMB. The more moderate
271 decay in Zone 2 might be the consequence of a solid-state phase transformation that is
272 considered in the ANEOS for dunite [Collins and Melosh, 2014]. This process does not occur in
273 the hydrodynamic models, because the shock pressure does not drop below the critical pressure.
274

Included in Figure 3 are the results from Pierazzo et al. [1997] for V_{imp}=10km/s and R_{imp} ranging between 0.4 and 10km, where the strength was not included. Our results for the hydrodynamic model, and the results from Pierazzo are in good agreement (Figure 3). The small differences between our results and the results from Pierazzo et al. [1997] are plausibly the direct consequence of using different cppr values (for R_{imp}=50km, cppr=25 while cppr=20 for Pierazzo et al. [1997]). Figure 3 illustrates that accounting for strength significantly reduces the intensity of the shock pressure. This indicates that building more sophisticated models is necessary to estimate the shock pressure evolution after a large impact, as suggested by Monteux and Arkani-Hamed [2016].

For large impacts, the thermal softening is an efficient process that may influence the shockwave propagation. Indeed, accounting for thermal softening changes the strength and, thus, the speed of the rarefaction wave, which may result in a different attenuation behavior. This process strongly depends on the pre-shocked temperature profile that is still poorly constrained during the early evolution of terrestrial planets. To illustrate the influence of the thermal softening, we have run two models with different pre-impact spherically symmetric temperature distributions, characterized by a cold boundary layer at the surface overlying a convective-type, adiabatic temperature within the mantle. The difference between these two models is the surface temperature that is 293K for the cold case and 500K for the hot case. Figure 4 shows that the thermal softening (as damage and acoustic fluidization) plays a minor role on the shockwave attenuation after a large impact. Accounting for thermal softening leads to a peak shock pressure decrease in Zone 1 and to an increase of the depth of Zone 1-Zone 2 transition. An initially hotter mantle only slightly enhances these 2 effects.

2.3 Scaling Laws

We have slightly modified the procedure by Monteux and Arkani-Hamed [2016]. By combining their near field and midfield, we reduce the number of parameters and make it easy to adopt the scaling laws in the impact heating of a terrestrial proto-plant during its accretion. We determine new scaling laws of shock pressure P for deriving universal scaling laws. From Figure 3, we

have identified 2 zones of particular interest: Zone 1 (associated to a peak shock pressure P_{Z1}) and Zone 2 (associated to a peak shock pressure P_{Z2}). This dichotomy is particularly pronounced in the models with strength.

We suggest two distinct scaling laws along the axis of symmetry to characterize the peak shock pressure in the model planet:

$$P_{Z1} = A_0 \exp(-A_1 D/R_{imp}) \quad (1a)$$

$$P_{Z2} = A_2 (D/R_{imp})^{-A_3} \quad (1b)$$

where D is the distance from the impact site, R_{imp} is the impactor radius. A_0 is the maximum shock pressure and A_1, A_2, and A_3 are constant obtained by fitting the results from the hydrocode models. All these parameters are impact velocity and impactor radius dependent. They also depend on the ray angle β. Zone 1 corresponds to a hemisphere centered at the impact site with radius D_{Z1}. Zone 2 corresponds to the mantle shell beyond D_{Z1}. Zone 2 lies between D_{Z1} and the CMB for the ray angle β <30°. The zone is limited by the surface of the impacted planet for β >30°(see Figure 2).

The scaling law used to fit the peak shock pressure decay within Zone 1 is different from the classical power-law that usually uses other empirical or semi-empirical relations in impact studies [e.g. Ahrens et al., 1977]. However it has two advantages: 1) with this formalism the peak shock pressure does not go to infinity as D/R_{imp} goes to 0 compared to other power law forms [e.g., Ruedas, 2017], and 2) the peak shock pressure decays relatively slowly for D/R_{imp}<3-4, which includes the "isobaric core" with slowly decaying shock pressure and the "pressure decay regime" regions proposed by Pierazzo et al., [1997]. On the other hand, the Zone 2 represents the far field region in the mantle where the shock pressure decays monotonically with distance from the impact site.

As the shock wave propagates in the mantle it creates a high pressure behind the shock front, which is determined on the basis of the Hugoniot equations. When the shockwave crosses the CMB, the peak shock pressure jumps from P_m (immediately above the CMB) to P_c (immediately

below the CMB) because of the abrupt changes in the physical parameters, as previously identified [e.g., Ivanov et al., 2010; Arkani-Hamed and Ivanov, 2014]. After this sudden increase, the peak shock pressure continues to decrease as the wave propagates inside the core, which is characterized by a separate scaling law:

$$P_{core} = A_4 (D/R_{imp})^{-A_5} \quad (1c)$$

where A_4 and A_5 are constants. Fitting the peak shock pressure from our numerical models along the ray paths shown in Figure 2 enables us to fully characterize the pressure increase experienced within the martian mantle and core. We note that a vertical impact on a spherically symmetric planet adopted in this study artificially enhances the shock pressure along the axis of symmetry in the core, hence Equation 1c overestimate the pressure near the axis of symmetry, while such an effect does not occur in the mantle (see the Discussion section below). Equations 1a, 1b and 1c will be used to fit the results from both the models with strength and the hydrodynamic models. The values of the different coefficients resulting from the corresponding fits are provided in the following sections. We would like to emphasize here that these scaling laws are only empirical and can be implemented in large-scale mantle models [e.g. Monteux and Arkani-Hamed, 2014] or in accretionary models [e.g. Monteux et al., 2014]. These scaling laws are determined by least square fitting to the results from the iSALE hydrocode models.

2.4 *Shock Wave Propagation in the Mantle: Effects of the Ray Angle*

During an impact, the maximum shock pressure is experienced at the impact site on the surface. Then the impact energy dissipates as the shockwave propagates within the model planet. Figure 5 shows that the maximum shock pressure A_0, in either the models with strength or the hydodynamic models, increases with the impact velocity and the impactor radius. The peak shock pressure is nearly constant within an almost hemispheric region of a radius 1-2 times the impactor radius, centered at the impact site (see Figure 3), which is coined as “isobaric core” by Pierazzo et al [1997]. We note that A_0 is the shock pressure at the impact site and it remains the same for all of the ray angles considered. It is used in our scaling law (Eq. 1a) to obtain the A_1 values from our models (Figure 6). Figure 5 shows the maximum shock pressure predicted from

368 the planar impact model [Melosh, 1989]. As detailed by Osinski and Pierazzo [2012], the planar
369 impact approximation yields an upper limit of the pressure expected during an impact event.
370 Hence, it is not surprising that our A_0 values are slightly smaller than the results from the planar
371 impact approximation.
372
373 Previous studies [Pierazzo et al., 1997, Monteux and Arkani-Hamed, 2016] monitored the
374 influence of the ray angle β of the shock wave, and found no significant angle dependence in
375 their results for β ranging between 0° (vertical) and 45°. Here we extend the investigation to β
376 values up to 80°. A_1 is the exponential factor (Eq. 1a), characterizing the ability of the upper
377 mantle to attenuate the shockwave as it propagates. For large A_1 values, the peak shock pressure
378 decreases rapidly with distance. Hence, higher A_1 values are expected for the models with
379 strength than for the hydrodynamic models. In Figures 6a and 6b, we present the A_1 values
380 obtained by fitting the results from iSALE models to Eq. 1a along different ray angles illustrated
381 in Figure 2. A_1 increases as a function of β, indicating that the peak shock pressure decreases
382 more efficiently with distance at large ray angles. This behavior is common to both models with
383 strength and hydrodynamics models. However, the increase is not significant for β values smaller
384 than 45°, as also mentioned by Pierazzo et al., [1997]. We note that the rays impinging the core
385 mantle boundary have β values smaller than 30^o, indicating that propagation of shock waves
386 inside the core is almost independent of the β values. Figures 6a shows that A_1 is weakly affected
387 by the impactor size for the range of impactors used in our study (*i.e.* 50<Rimp<200km). For
388 larger impactors (not studied here), one can expect an influence of the impacted protoplanet
389 curvature on the shockwave propagation. However, Figures 6b shows that A_1 is more sensitive to
390 the impact velocity. Pierazzo et al. [1997] showed that the power-law exponent used to fit the
391 angle dependency (for β ranging between 0° and 45°) was increasing with the velocity. From our
392 results (for β ranging between 0° and 80°) it is difficult to extract such a tendency.
393
394 For the large ray angles, the path followed by the shockwave is shallower (Figure 2). The shock
395 wave propagating through shallower regions will cross material where the pressure and the
396 uncompressed target density are smaller in average compared to shock wave propagating along
397 the axis of symmetry. As a consequence, along small ray angle paths, the deformation is more
398 difficult than along large ray angle paths. In addition, in shallower regions a significant part of

399 the impact energy is dissipated during processes such as the excavation or the post-impact
400 rebound. Finally, the interference of the direct pressure wave with the rarefaction wave that is
401 reflected at the surface reduces the amplitude of the shock pressure [Melosh, 1989; Arkani-
402 Hamed, 2005; Louzada and Stewart, 2009]. The consequence of these factors is that the isobaric
403 surfaces are slightly elliptical with vertical major axis rather than spherical.
404
405 As previously mentioned, the shock wave decay rate with distance should be more rapid for the
406 model with strength compared to the hydrodynamic models (as illustrated in Figure 3). Figures
407 6a and 6b confirm this point by showing that A_1 values are larger for models with strength than
408 for hydrodynamic models for all β values. The correlation coefficients obtained by fitting our
409 hydrocode data with the scaling laws from Eqs. 1 a, b and c show that our choice is relevant. The
410 correlation coefficients are close to 0.9 for all the range of impactor radii and impact velocities
411 used in our models (except for V_{imp}=20km/s). The correlation coefficients are even higher for β
412 values smaller than 65°. The correlation coefficients are also larger in the models with strength
413 than in the hydrodynamic models because the dichotomy between Zone 1 and Zone 2 is more
414 pronounced in the models with strength than in the hydrodynamic models (See Figure 3).
415
416 In our study, the distance D from the impact site is normalized to the impactor radius R_{imp} to
417 eliminate the dependence on the size of the projectile. Figure 7 illustrates peak shock pressure
418 profiles along a ray angle of β =36° meaning that the ray does not cross the CMB (see Figure 2).
419 Figure 7 shows that the boundary between Zone 1 and Zone 2 depends on both the impactor size
420 and the impact velocity, hence the total pressure (shock plus lithostatic) through the Equation of
421 State adopted in the hydrocode models. This suggests a relation between the observed transition
422 and a phase change in the Equation of State from our iSALE models. The Zone 1 - Zone 2
423 boundary occurs at a constant distance close to 10 times the radius of the impactor for the range
424 of impactor sizes studied (Figure 7, left). In the cases shown in Figure 7, β is close to the critical
425 value of 30° where the ray crosses the CMB (Figure 2). As R_{imp} increases, the minimal value
426 D/R_{imp} for which the shockwave crosses the CMB decreases from 34 (for R_{imp}=50 km, black
427 curve) to 8.5 (for R_{imp}=200 km, blue curve). At this singular point (Figure 7, left), a small jump
428 of the peak pressure occurs because of the reflection of the shock waves with β <30° at the CMB.
429 The ratio of the isobaric core radius to the projectile radius weakly depends on the impact

velocity, as also concluded by Pierazzo et al. [1997]. For the range of impact velocities considered, the Zone 1 - Zone 2 boundary ranges between 7 and 15 times the radius of the impactor (Figure 7, right). The small peak shock pressure jumps identified in Figure 7 (left) for large impactors does not occur here because of the small, 50 km, impactor radius.

Once the shockwaves enter into Zone 2, the peak pressure continues to decrease. Figures 8a and 8b show the dependency of A_2 on the ray angle (see Eq. 1b). Because peak shock pressure decreases more rapidly with distance in the models with strength than in the hydrodynamic models (see Figure 3), A_2 values are smaller in the models with strength than in the hydrodynamic models. Also, A_2 only slightly decreases with the ray angle β in both cases. For all impact velocities and impactor radii studied here, the A_2 values obtained from the models with strength are nearly constant up to the values of β close to 65°. For $\beta > 65°$, the data is more scattered (see discussion at the end of the section). For the large impactor, R_{imp}=200km, the evolution of A_2 as a function of β is significantly different. This is probably due to the fact that, in that case, Zone 1 overlaps the CMB.

Figures 9a and 9b show the relationship between A_3 (see Eq. 1b) and the ray angle β. As for A_1, A_3 is smaller in the models with strength than in the hydrodynamic models. This feature is related to the higher shear strength in the models with strength, which consumes a portion of the impact energy to plastically deform the impacted material. Again, the more moderate decay in Zone 2 (i.e. smaller A_3 values) in models with strength compared to hydrodynamic models might be the consequence of a solid-state phase transformation that is considered in the ANEOS for dunite [Collins and Melosh, 2014]. Apart from this difference, both models behave similarly. Figures 9a and 9b show that A_3 slightly increases with β up to $\beta \approx 65°$ indicating that the peak shock pressure decreases more efficiently with distance at large ray angles. From the results illustrated in Figure 9b, the A_3 coefficient does not significantly depend on the impact velocity. However, Figure 9a shows that the tendencies described earlier are completely different for $R_{imp} \geq 150$ km. Indeed, for large impactors, the size of Zone 2 is significantly reduced and the impacted hemisphere mainly consists of Zone 1 and the metallic core within the ray angle less than 30°.

To illustrate the dependencies of A_1, A_2 and A_3 on β, we express them as $A_i = A_6 \exp(A_7 \beta)$ where i denotes 1, 2, or 3 (see legend boxes in the corresponding figures). Figures 6, 8 and 9 show small values for A_7, typically ranging between 10^{-2} and 10^{-3}. This confirms that the shock wave propagation weakly depends on the ray angle that is ranging between 0° (vertical) and 45°, as already concluded by previous studies [Pierazzo et al., 1997, Monteux and Arkani-Hamed, 2016]. This can be extended for β up to 60° on the basis of Figures 6, 8 and 9. For the hydrodynamic models the trend is similar although the iSALE data are more dispersed. Figures 8 and 9 also show that for R_{imp} values larger than 150 km, the trend is less clear than for small impactors. As already mentioned, we attribute this feature to the overlap between Zone 1 and the CMB, which leads to the progressive disappearance of Zone 2 as R_{imp} increases. These differences are confirmed by the correlation coefficients that are larger for small impactors and are generally higher for the models with strength than for the hydrodynamic models where the iSALE data is more dispersed.

Figures 8 and 9 also exhibit a large variability for β values larger than 65°. For these large β values the shock waves propagate through shallower regions (see Figure 2) where the total pressure is much smaller than that in the deep mantle. Moreover, in the shallowest region the largest initial impact is followed by multiple smaller impacts caused by ejecta fall back. Finally, the near surface region is also affected by the wave reflected at the surface that interferes with the direct wave and complicates the determination of the peak shock pressure [Melosh, 1989; Arkani-Hamed, 2005; Louzada and Stewart, 2009]. These 3 effects may explain the variability of the A_1, A_2, A_3 constants for large β values.

2.5 Effects of the CMB

The distinctly different physical properties of the mantle and the core have two major effects on the shock wave as it passes from the mantle to the core. The shock pressure increases abruptly as seen in Figure 3, and a shock ray bends, obeying the Snell's law. Here we discuss each of these two effects.

Because the core radius is half the size of the impacted planet, the shock waves encounter the CMB only for β values smaller than 30 degrees (Figure 2). Figure 10 shows the ratio of the shock pressure immediately above the CMB, P_m, to that immediately below the CMB, P_c, in the impacted hemisphere. Both are calculated along a straight line determined by a ray angle and at the grid points of the hydrocode models immediately above and below the CMB, respectively. We note that P_m and P_c are actually the pressures slightly off the shock ray, hence are approximations to the actual pressures on the ray. A given shock ray bends toward the axis of symmetry as it crosses the CMB and the refraction angle determined through the Snell's law is smaller than the incident angle (see below). The bend is more pronounced at higher ray angles.

To connect the peak shock pressure between the mantle and the core we fit the ratio P_c/P_m as a function of the ray angle β with a quadratic expression for the models with strength:

$$P_c/P_m = b_1+b_2\beta+b_3\beta^2 \quad (2a)$$

and a linear expression for the hydrodynamic models:

$$P_c/P_m = b_4+b_5\beta \quad (2b)$$

where b_1, b_2, b_3, b_4 and b_5 are constant. The values of these constants for both models and as a function of R_{imp} and V_{imp} are listed in Table 3. The corresponding results are illustrated in Figures 10a and 10b. We emphasize here that the equations 2a and 2b used to fit the pressure jump as a function of the ray angle β are chosen empirically according to our results illustrated in Figure 10 and b.

For all the impact velocities and impactor radii used in our models, the behavior is quite similar, although the shockwave that arrives at the CMB has much higher amplitude in the hydrodynamic case than in the models with strength (Figure 3). Figure 10 shows that the pressure jump at the CMB is more pronounced in the models with strength than in the hydrodynamic models, regardless of the amplitude of the arriving shockwave. Because the pressure jump at the CMB is likely related to the amplitude of the arriving shockwave for a given model, our results

emphasize the importance of the impacted material properties on the amplitude of the pressure jump.

For large impactors (R_{imp}>150 km) and for β values smaller than 30°, we have shown that Zone 1 directly interferes with the impacted planet's core thus leading to a disappearance of Zone 2. Above this critical value of β>30°, even if the direct shockwave does not cross the core (Figure 2), one can expect that the transition from Zone 1 to Zone 2 would still be identified in our models. However, Figure 8a (bottom panels) and Figure 9a (bottom panels) also show a different behavior for large impactors for β>30°. We attribute this phenomenon to the interaction of the direct shockwave with the core which produce a variety of diffracted and reflected shockwaves that affect the peak shock pressure far from the impact site and for β>30°. As the shockwave behavior is completely different, our scaling laws for A_2, A_3 and P_c/P_m proposed in Eqs. 1b, 2a and 2b are less viable. The tendency for A_2 and A_3 is difficult to identify from our results (Figure 8a and Figure 9a (bottom panels)) and this complexity probably illustrate the complexity of the shockwave propagation far from the impact site.

The incident angle of a shock ray at the CMB increases from 0^o to 90^o as the ray angle β increases from 0^o to 30^o. The refraction angle of a given shock ray is determined on the basis of the Snell's law,

$$U_m / \sin \gamma_m = U_c / \sin \gamma_c \quad (3)$$

where U_m and U_c are the shock wave velocities in the mantle and the core, γ_m is the incident angle, and γ_c is the refraction angle. U_m and U_c are determined from our numerical models (see the next section).

2.6 Shock Wave Propagation in the Core

Figure 11 shows the dependency of the coefficients A_4 and A_5 in Eq. 1c on V_{imp} and R_{imp} determined along the axis of symmetry using the hydrocode models. A_4 shows a power-law

552 behavior while A_5 shows almost linear dependency, especially those associated with the models
553 with strength.
554
555 For a given ray angle β we calculate the incident and the refraction angles at CMB, hence the
556 corresponding shock ray path in the core, assuming linear. The peak shock pressure decay along
557 this ray path is determined from Eq. 1c, where D is the distance from the impact site to a point in
558 the core measured along the ray path assuming that A_4 and A_5 are independent of the ray angle.
559 Figure 12 shows the distance of the peak shock pressure from the impact site in the impacted
560 hemisphere of the mantle and the entire core versus the time since the impact. Table 4 lists the
561 corresponding shock wave velocity in the mantle and the core. The shock wave velocities vary
562 slightly among the models. More importantly, the velocity in the core is consistently lower than
563 that in the mantle, indicating that the refracted ray angle is always smaller than the incident ray
564 angle.
565
566 **3. Comparison of the Scaling Law Models with the iSALE Models**
567
568 Before implementing our scaling laws to the accretion of a planet it is required to compare the
569 scaling law models with the iSALE models. Here we compare the hydrocode models and the
570 models with strength to the corresponding models determined using our scaling laws for the
571 impact velocity of 10km/s and the impactor radius of 50km (Figures 13 a and b). In the scaling
572 law models the refracted angles of the shock rays at the CMB are determined by the Snell's law.
573 Hence, the shock pressure is not estimated in the equatorial region of the core where no refracted
574 wave propagates. This results in the distinct lack of shock pressure in the equatorial part of the
575 core and in the lower mantle beneath the shock ray that is tangent to the core mantle boundary.
576 Several other features are not modeled by the scaling laws because we do not consider the
577 reflection at the CMB and at the surface or the reflection and refraction at the antipodal CMB,
578 which are included in solving the shock dynamic equation in the hydrocode models. .
579
580
581 Figure 13 (right panel) shows the relative difference between the two models. For the impacted
582 hemisphere, the mean errors are 13% within the mantle and 14% within the core for the model

583 with strength, and 10% within the mantle and 12% within the core for the hydrodynamic model.
584 The fact that iSALE model combines both direct and indirect waves, while our model shows
585 only the direct wave could contribute to the error between our scaling law parameterization and
586 the iSALE data. The error pattern is similar in both the hydrodynamic and strength models. As
587 mentioned above, the direct shock pressure within the core for β values larger than 30° is not
588 determined by the scaling laws. The shock pressure of the hydrocode model in this region must
589 be due to the secondary shock waves that are reflected at the surface and then refracted at the
590 CMB. The scaling law models overestimate the peak shock pressure close to the impact site
591 (Zone 1) where the error can locally reach 50 %. However, despite the large peak shock pressure
592 range in this region, our scaling laws provide a first order approximation to the hydrocode
593 models.
594
595 An impact generates two compressional shockwaves, one propagates downward in the planet and
596 the other propagates upward in the penetrating impactor. The latter reaches the top of the
597 impactor, and reflects back and propagates downward as a rarefaction wave. The turbulence
598 induced by the compressional wave in a given location inside the planet is diminished by the
599 trailing rarefaction wave. This limits the thickness of the entire shock front with appreciable
600 turbulence. The velocity of the rarefaction wave is higher than that of the original down going
601 compressional wave, because the rarefaction wave propagates inside the penetrating impactor in
602 the early times and then inside the planet that is already set in motion by the initially down going
603 compressional wave. At a shock wave velocity of about 8 km/s, the passage of the entire shock
604 front at a given location takes less than a minute for the largest impactor of 200 km considered in
605 this study, and much shorter for other impactors. A given location in the mantle experiences
606 more than one shock wave, such as the shock wave reflected at the surface and that reflected at
607 the CMB. However, these shock waves have low amplitudes because they travel longer
608 distances than the direct wave and they arrive at much later times relative to the direct pressure
609 wave. They rarely interfere with the direct wave except near the surface and near the CMB. In
610 the case of the core, parts of the antipodal core is shocked twice, first by the direct wave that is
611 refracted at the CMB of the impacted hemisphere beneath the impact site and second by the
612 shock wave reflected at the CMB of the antipodal hemisphere. The first wave travels a shorter
613 distance than the second one, hence passes a given location sooner than the arrival of the

reflected wave. As in the case of the mantle, there is negligible interaction between these two waves, except for very close to the antipodal CMB. In general, a given location experiences multiple pressure increases due to the multiple reflected and refracted waves that travel through the planet's interior. However, the peak pressure is due to the direct shockwave.

4. Impact heating

During the decompression, a fraction of the energy is converted into heat [Bjorkman and Holsapple, 1987]. The temperature increase has been related to the shock pressure [e.g., Watters et al., 2009] as well as to the particle velocity [e.g., Gault and Heitowit, 1963]. The shock pressure in a given location diminishes within a time scale that is much shorter than the cooling timescale of the impact induced thermal anomaly. Although secondary shock waves lead to local pressure increase, the corresponding temperature increase is negligible compared to that of the direct shock wave. Here we only consider the direct shock heating in our estimation of the impact induced temperature increase.

The impact heating induced by the shockwave propagation is determined by implementing our scaling laws within the theoretical model proposed by Watters et al. [2009]

$$\Delta T(P_\delta) = \left(\frac{P_\delta}{2\rho_0 S}(1 - f^{-1}) - \left(\frac{C}{S}\right)^2 [f - \ln f - 1]\right)/c_p \quad (4)$$

$$f(P_\delta) = -\frac{P_\delta}{\beta}\left(1 - \sqrt{\frac{2P_\delta}{\beta} + 1}\right)^{-1} \quad (5)$$

$$\beta = \frac{C^2\rho_0}{2S} \quad (6)$$

where P_δ is the shock-induced pressure, ρ_0 is the density prior to the shock compression and c_p is the heat capacity of the impacted material (see values in Tab. 1). The shock pressure implemented in Eqs. 4, 5 and 6, is the shock-induced pressure predicted by our scaling laws (Eqs. 1 and 2). Figure 14 shows the temperature increase obtained using our scaling laws for both the hydrodynamic model and the model with strength for V_{imp}=10km/s and R_{imp}=50 km (top

643 panels) and V_{imp}=10km/s and R_{imp}=150 km (bottom panels). As mentioned before, the shock
644 pressure is not estimated by the scaling laws where no refracted wave propagates (i.e. in the
645 equatorial region of the core and the lower part of the mantle beneath the shock ray that is
646 tangent to the CMB). Hence, we cannot estimate the post-impact temperature increase in these
647 regions (illustrated by black areas in Figure 14). This figure shows that for a 50 km radius
648 impactor, the region with significant impact heating is localized in a small shallow volume. For a
649 150 km impactor, a larger fraction of the impacted mantle is affected. Below the impact site the
650 temperature increase can reach ≈1900K for both the hydrodynamic model and the model with
651 strength. The largest temperature increase is localized in Zone 1 and the temperature increase in
652 Zone 2 is weaker. The main difference between the two rheologies is the depth of the impact
653 temperature increase, which is deeper in the hydrodynamic model than in the model with
654 strength, because the pressure decay is more rapid in the model with strength (Figure 6 a, bottom
655 left panel). Moreover, the regions with increased temperature have shapes that are more prolate
656 than spherical, because of the influence of the β angle on the pressure decay in Zone 1. The
657 difference in the expression of the pressure decay between the two models as a function of β
658 should lead to a difference in sphericity (Figure 6 a). However, the difference is not significant in
659 the cases illustrated in Figure 14.
660
661 **5. Discussion and Conclusions.**
662
663 We have modeled the shock pressure distributions inside the impacted hemisphere of a
664 differentiated Mars size planet using 2D axi-symmetric hydrocode simulations (iSALE-2D) for
665 vertical impacts with impact velocities of 5–20 km/s and impactor radii ranging from 50 to 200
666 km. From these hydrocode simulations, we have observed a distribution of the peak shock
667 pressure within the impacted mantle and proposed a mathematical formalism adapted to this
668 distribution: a first zone (Zone 1) where the peak shock pressure decreases exponentially and a
669 second zone (Zone 2) where the peak shock pressure decrease follows a power-law. With this
670 formalism, the peak shock pressure does not go to infinity as D/R_{imp} goes to 0, and the peak
671 shock pressure decays relatively slowly from the impact site to D/R_{imp}=3-4, which includes the
672 canonical "isobaric core" with slowly decaying shock pressure with distance from the impact site

673 and the "pressure decay regime" region proposed by Pierazzo et al., [1997]. We have shown
674 that the ray angle β has minor influence on the pressure decay pattern for β<65-70°.
675
676 The most important contribution to the peak shock pressure distribution is related to the rheology
677 of the material. Adopting a model where the impacted mantle is treated using models with
678 strength can result in a significant decrease of the peak shock pressure compared to that of the
679 hydrodynamic models. This difference in behavior occurs principally in the shallower zone
680 (Zone 1) while in Zone 2 the behavior is similar in both models. We have shown that the peak
681 shock pressure is about an order of magnitude smaller at the bottom of the Zone 1 in the models
682 with strength compared to that in the hydrodynamic models.
683
684 The characteristic of the peak shock pressure in Zone 1 has important consequences on the peak
685 shock pressure in Zone 2, since it determines the pressure in the upper part of Zone 2. Also, the
686 mantle rheology affects the peak shock pressure at the CMB. We have combined our shock-
687 pressure scaling laws with the formalism proposed by Watters et al. [2009] to determine the
688 impact heating of a differentiated Mars model by a large impactor. Our results show that the
689 mantle rheology governs the impact heating of a planet and the impact heating may be
690 overestimated when the material strength is not accounted for.
691
692 The martian rheology and its evolution since Mars formation are poorly constrained. However,
693 the two models used in our study (hydrodynamic and with strength) enable us to cover a range of
694 rheology models compatible with different stages of the Martian evolution. Our hydrodynamic
695 models where the mantle is considered as an inviscid fluid may be an interesting proxy to
696 characterize the impact heating during a magma ocean stage [Monteux et al., 2016]. On the other
697 hand, our models with strength are more appropriate to characterize the large impact
698 consequences within a solidified and cold Mars [Watters et al., 2009]. Our results show that the
699 depth of the heated zone is different in the two cases (Figure 14) with a larger thermal anomaly
700 in the hydrodynamics models than in the models with strength as the pressure decay is more
701 rapid in the latter case. In both cases, the shape of the impact-heated region is prolate because of
702 the influence of β on the pressure decay. These effects need to be accounted for in accretionary

703 models especially when about $3x10^5$ planetesimals of ~100 km in diameter are needed to build a
704 Mars size planet.
705
706 As illustrated in Figure 13, our parameterized approach is associated to a mean error
707 between our scaling laws and the direct results obtained by the iSALE models that ranges form
708 10 to 14% within the impacted hemisphere. As a consequence, the temperature increase derived
709 from our scaling laws is also associated to this error range. Nonetheless, in the light of the
710 incertitude that goes with our understanding of the early Solar System history and our knowledge
711 of the effects of large impacts, our parameterized approach to calculate the temperature increase
712 within a differentiated Mars-size protoplanet can be considered as a first order estimation.
713
714 As a consequence, the next step toward a better understanding of the early evolution of terrestrial
715 planets is to implement more realistic rheological models in the hydrocode simulations. Such an
716 effort would lead to more reliable scaling laws that could easily be implemented in accretion
717 models to characterize the influence of large impacts on the martian mantle dynamics [e.g.
718 Roberts and Arkani-Hamed, 2012, 2017] or on other terrestrial planets [e.g. Roberts and
719 Barnouin, 2012]. As large impacts are not isolated phenomena during the late regimes of
720 planetary accretions, the scaling laws we have developed are suitable to be implemented in
721 thermal evolution models that consider the accretion histories of growing planets [*e.g.* Monteux
722 et al., 2014, Arkani-Hamed, 2017].
723
724 The followings are some shortcomings that require improvements of our scaling laws in the
725 future to be better suited for shock waves travelling inside an actual planet, rather than the simple
726 two-layered planet model where a uniform mantle overlies a uniform core.
727
728 • We have considered vertical impacts, whereas majority of impacts during the accretion of
729 a planet is oblique. The peak shock pressure produced by an oblique impact along the
730 vertical direction beneath the impact site depends on the sine of the impact angle relative
731 to the local horizon (see Figure 3 of Pierazzo and Melosh, [2000]). This implies a shock
732 pressure reduction by a factor of ~0.71 for the most probable impact angle of 45^o
733 [Shoemaker, 1962] compared to that of a vertical impact, assuming that all other

parameters are equal. Moreover, a vertical impact on a spherically symmetric planet preserves the axial symmetry. Because the shock wave velocity in the core is smaller than that in the mantle, the axial symmetry results in the convergence of the refracted wave at the CMB of the impacted hemisphere toward the axis in the core, thus artificially increasing the shock pressure near the axis. However, the near axis enhancement of the shock pressure is negligible except very close to the antipodal CMB [Ivanov et al., 2010; Arkani-Hamed and Ivanov, 2014]. We also note that this artifact does not occur in the mantle because the shock rays are diverging away from the axis of symmetry. It is desirable to adopt oblique impacts in investigating the accretion of a planet. In an oblique impact, the axial symmetry is replaced by a plane symmetry, which avoids the convergence of the waves toward the axis in the expense of introducing more complex and computationally intensive three-dimensional (3D) calculations, besides the substantial increase of the grid points in the computation domain.

- The distance travelled by a shock wave from the impact site to a given point in the planet is approximated by a straight line, D. In our simplified two-layered planet model with a uniform mantle overlying a uniform core, the first arrival shock wave travels in quiescent medium, hence the shock rays are straight lines until they interact with the core mantle boundary where they bend according to the Snell's law. Inside a real planet the rays are actually curved due to the pre-impact non-uniform density and temperature gradients in the interior of the planet. Because of the ray curvature a wave travels longer to reach an off axis location in the interior than D. Therefore, our model slightly over estimates the shock pressure experienced in that location. Moreover, because of the ray curvature an incident angle at the CMB and the corresponding refraction angle could be slightly different than those determined by the straight line approximation. However, the core radius is about one half of the planet radius, and the angle β is always smaller than 30°. Bearing in mind that the shock ray along the axis of symmetry is a straight line, the departure of the shock rays from the corresponding straight lines is negligible for these β values. As also mentioned above, the shock wave propagation weakly depends on the β angle that is ranging between 0° (vertical) and 45°, which is already concluded by previous studies [Pierazzo et al., 1997, Monteux and Arkani-Hamed, 2016]. More

765 importantly, providing scaling laws along straight lines, rather than along shock rays,
766 helps to easily determine the shock pressure in the entire region.
767
768 • We have considered only direct shock waves to determine our scaling laws. Because the
769 laws are based on shock ray theory, they can be used to determine the pressure of
770 secondary shock waves, such as those reflected at the surface and those reflected at the
771 antipodal CMB of the core [Arkani-Hamed and Ivanov, 2014]. In general a reflect wave
772 arriving at a location travels longer and is weaker than a direct wave. However, because
773 of the zero pressure boundary condition at the surface the reflected wave is rarefaction
774 and upon interference with the direct compressional wave effectively reduced the
775 pressure experienced at a given location close to the surface [Melosh, 1989; Arkani-
776 Hamed, 2005; Louzada and Stewart, 2009]. The interference of the direct and secondary
777 waves is not considered in our present study.
778
779 • The size of the Zone 1 depends on the impactor size. For large impactors Zone 1 directly
780 interferes with the core, and Zone 2 does not exist. For example, there is no Zone 2 for β
781 values smaller than 15° when the impactor is larger than 150 km in radius. We propose
782 the following procedure to estimate the shock pressure distribution inside the mantle and
783 the core of a planet using our scaling laws. The impact-induced temperature increase
784 may then be determined using, for example Watters et al [2009] model.
785
786 • Consider a terrestrial planet with a radius R_p and a core radius R_c that is impacted by an
787 impactor of radius R_{imp}. We assume that the Zone 1 is a hemisphere with a radius R_1 = 10
788 x R_{imp} centered at the impact site. There is no interaction of Zone 1 with the core for R_1
789 $< (R_p - R_c)$, and the equations provided in this paper are valid. This is also the case for
790 any shock wave specified by a ray angle β when $\sin(\beta) > R_c/R_p$. For $R_1 > (R_p - R_c)$, Zone
791 1 may interact with the core. Because the shock wave velocity is greater than the particle
792 velocity, it takes time for the CMB to deform, during which the shock wave has already
793 entered the core, hence the incident shock wave impinges on a undeformed spherical
794 core. Therefore, a Zone 2 exists for the colatitudes greater than θ_1, where $\cos(\theta_1) = (R_p^2$

795 + $R_c^2 - R_1^2) / 2 R_p R_c$, and the equations provided in this paper are still valid. Zone 1
796 interacts with the core only for the colatitudes smaller than θ_1.
797
798
799 **Acknowledgements**
800
801 This research was supported by the Auvergne Fellowship program to JM, and by the Natural
802 Sciences and Engineering Research Council (NSERC) of Canada to JAH. We gratefully
803 acknowledge the developers of iSALE (www.isale-code.de), particularly the help we have
804 received from Gareth S. Collins. We also would like to thank the two anonymous reviewers for
805 their constructive comments. This paper is Laboratory of Excellence ClerVolc contribution no.
806 XX.
807
808

References:

Agnor, C. B., and E. Asphaug (2004), Accretion efficiency during planetary collisions, Astrophys. J., 613, L157–L160.

Agnor, C. B., R. M. Canup, and H. F. Leviston (1999), On the character and consequences of large impacts in the late stage of terrestrial planet formation, Icarus, 142, 219–237.

Ahrens, T.J., O'Keefe, J.D., Merrill, R.B., 1977. Equations of State and Impact-Induced Shock-Wave Attenuation on the Moon. Impact and Explosion Cratering, Perga- mon Press, Elmsford, N.Y., pp. 639–656.

Ahrens, T.J., J.D., O'Keefe, (1987). Impact on the Earth, ocean and atmosphere. Int. J. Impact Eng. 5, 13–32.

Amsden, A., Ruppel, H., and Hirt, C. (1980). SALE: A simplified ALE computer program for fluid flow at all speeds. Los Alamos National Laboratories Report, LA-8095:101p. Los Alamos, New Mexico:LANL.

Arkani-Hamed, J., (2005), Magnetic crust of Mars, J. Geophys. Res. 110, E08005, doi:10.1029/2004JE002397.

Arkani-Hamed, J. (2017), Formation of a solid inner core during the accretion of Earth, J. Geophys. Res. Solid Earth, 122,doi:10.1002/2016JB013601.

Arkani-Hamed, J., Olson, P., (2010a). Giant impact stratification of the martian core. Geophys. Res. Lett. 37, L02201. http://dx.doi.org/10.1029/2009GL04141.

Arkani-Hamed, J., Olson, P., (2010b). Giant impacts, core stratification, and failure of the martian dynamo. J. Geophys. Res. 115, E07012.

Arkani-Hamed, J., and B. Ivanov (2014), Shock wave propagation in layered planetary embryos, Phys. Earth Planet. In., 230,45–59.

Barr, A., Citron, R., (2011). Scaling of melt production in hypervelocity impacts from high-resolution numerical simulations. Icarus 211, 913–916.

Benz, W., Cameron, A.G.W., Melosh, H.J., (1989). The origin of the Moon and the single-impact hypothesis III. Icarus 81, 113–131.

Bierhaus, M., K. Wünnemann, and D. Elbeshausen, (2012). Numerical modeling of basin-forming impacts: implications for the heat budget of planetary interiors, Large meteorite impacts and Planetary evolution V. LPI Contribution No. 1737.

839 Bierhaus, M., K. Wünnemann, and B.A. Ivanov, (2013). Affect of core rheology on shock wave
840 propagation in planetary scale impacts, 43rd Lunar and Planetary Science Conference. Abstract #
841 2174.pdf.
842 Bjorkman, M.D., Holsapple, K.A., (1987). Velocity scaling impact melt volume. Int. J. Eng. 5,
843 155–163.
844 Bottke W. F., Nolan M. C., Greenberg R., and Kolvoord R. A. (1994). Collisional lifetimes and
845 impact statistics of near-Earth asteroids. In Hazards due to comets and asteroids, edited by
846 Gehrels T. Tucson, Arizona: The University of Arizona Press. pp. 337–357.
847 Chambers, J.E., Wetherill, G.W., (1998). Making the terrestrial planets: N-body integrations of
848 planetary embryos in three dimensions. Icarus 136, 304–327.
849 Chambers, J.E., (2004). Planetary accretion in the inner Solar System, Earth Planet. Sci. Lett.
850 223, 241–252.
851 Chambers, J. E. (2013), Late-stage planetary accretion including hit-and-run collisions and
852 fragmentation, Icarus, 224, 43–56.
853 Collins, G. S., Melosh, H. J., 2014, Improvements to ANEOS for multiple phase transitions. 45th
854 Lunar and Planetary Science Conference, 2664.
855 Curran, D. R., D. A. Shockey, L. Seaman,and M. Austin, (1977) Mechanics and models of
856 cratering in earth media, in Impact and Explosion Cratering, edited by D. J. Roddy, R. O. Pepin,
857 and R. B. Merrill, pp. 1057-1087, Pergamon, New York.
858 Frey, H., 2008. Ages of very large impact basins on Mars: Implications for the late heavy
859 bombardment in the inner Solar System. Geophys. Res. Lett. 35, L13203.
860 Gault, D. E., and E. Heitowit (1963), The partition of energy for hypervelocity impact craters
861 formed in rock, Proceedings of the 6th Hypervelocity Impact Symposium, *2*, 419–456.
862 Ghods, A., and J. Arkani-Hamed (2011), Effects of the Borealis impact on the mantle dynamics
863 of Mars, Phys. Earth Planet. Inter., 188, 37–46.
864 Holsapple, K. A. (1993), The scaling of impact processes in planetary sciences, Annu. Rev.
865 Earth Planet. Sci., 21, 333– 373
866 Ivanov, B. A., Deniem, D., and Neukum, G. (1997). Implementation of dynamic strength models
867 into 2D hydrocodes: Applications for atmospheric breakup and impact cratering. International
868 Journal of Impact Engineering, 20:411-430.

869 Ivanov, B.A., H.J. Melosh, and E. Pierazzo, (2010). Basin-forming impacts: Reconnaissance
870 modeling, Geological Society of America, Special Paper 465, 29-49.
871 Kaula, W.M., (1979). Thermal evolution of Earth and Moon growing by planetesimal impacts. J.
872 Geophys. Res. 84, 999–1008.
873 Kendall, J.D., Melosh, H.J., (2016). Differentiated planetesimal impacts into a terrestrial magma
874 ocean: fate of the iron core. Earth Planet. Sci. Lett. 448, 24–33.
875 Kokubo, E., and H. Genda (2010), Formation of the terrestrial planets form protoplanets under a
876 realistic accretion condition, Astrophys. J. Lett., 714, L21–L25.
877 Kokubo, E. and S. Ida, (2000). Formation of protoplanets from planetesimals in the solar nebula,
878 Icarus 143, 15–27.
879 Kraus, R.G., Senft, L.E., Stewart, S.T., (2011). Impacts onto H2O ice: Scaling laws for melting,
880 vaporization, excavation, and final crater size. Icarus 214, 724–738.
881 Leinhardt, Z.M., Stewart, S.T., (2009). Full numerical simulations of catastrophic small body
882 collisions. Icarus 199, 542–559.
883 Louzada, K.L., and S. T. Stewart, (2009). Effects of planet curvature and crust on the shock
884 pressure field around impact basins, Geophys. Res. Letter., 36, L15203.
885 Melosh, H. J. (1989), Impact Cratering: A Geologic Process, Oxford Univ. Press, New York.
886 Mitani, N. K. (2003), Numerical simulations of shock attenuation in solids and reevaluation of
887 scaling law, *J. Geophys. Res.,* 108, (E1), 5003, doi:10.1029/2000JE001472.
888 Monteux J, Arkani-Hamed J (2014) Consequences of giant impacts in early Mars: Core merging
889 and Martian dynamo evolution. J Geophys Res 119:480–505
890 Monteux, J., G. Tobie, G. Choblet, and M. Le Feuvre (2014), Can large icy moons accrete
891 undifferentiated?, Icarus, 237, 377–387
892 Monteux, J., and J. Arkani-Hamed (2016), Scaling laws of impact induced shock pressure and
893 particle velocity in planetary mantle, *Icarus*, 264, 246–256.
894 Monteux, J., Andrault, D. & Samuel, H (2016). On the cooling of a deep terrestrial magma
895 ocean. Earth Planet. Sci. Lett. 448, 140–149.
896 Ohnaka, M., 1995. A shear failure strength law of rock in the brittle-plastic transition regime.
897 Geophys. Res. Lett. 22, 25–28.
898 Osinski, G.R. and Pierazzo, E. (2012), Impact Cratering: Processes and products, Blackwell
899 Publishing Ltd. 330 pp.

900 Pierazzo, E., Vickery, A.M., and Melosh, H.J., (1997). A re evaluation of impact melt
901 production. Icarus 127, 408–423.
902 Pierazzo, E., and H. J. Melosh, (2000). Melt Production in Oblique Impacts, Icarus 145, 252–
903 261.
904 Pierazzo, E., and H. J. Melosh (2000), Understanding oblique impacts from experiments,
905 observations, and modeling, Annu. Rev. Earth Planet. Sci., 28, 141–167.
906 Pierazzo, E. et al., (2008). Validation of numerical codes for impact and explosion cratering:
907 Impacts on strengthless and metal targets. Meteorit. Planet. Sci. 43 (12), 1917–1938.
908 Potter, R.W.K. et al., 2012. Constraining the size of the South Pole-Aitken basin impact. Icarus
909 220, 730–743.
910 Rafikov, R.R., (2003). The growth of planetary embryos: Orderly, runaway, or oligarchic, The
911 Astron. J., 125, 942–961.
912 Raymond, S.N., T. Quinn, and J. I. Lunine, (2006). High-resolution simulations of the final
913 assembly of Earth-like planets, Terrestrial accretion and dynamics, Icarus 183, 265–282.
914 Ricard, Y., Bercovici, D. and Albarède, F. (2017). Thermal evolution of planetesimals during
915 accretion, Icarus, 285, 103-117.
916 Ricard, Y., Srámek, O., Dubuffet, F., (2009). A multi-phase model of runaway core-mantle
917 segregation in planetary embryos. Earth Planet Sci. Lett. 284, 144–150.
918 Rivoldini, A., Van Hoolst, T., Verhoeven, O., Mocquet, A., Dehant, V., (2011). Geodesy
919 constraints on the interior structure and composition of Mars. Icarus 213, 451–472.
920 Robbins, S.J., Hynek, B.M., Lillis, R.J., & Bottke, W.F. (2013). Large impact crater histories of
921 Mars: the effect of different model crater age techniques, Icarus, 225, 173–184.
922 Roberts, J.H., and J. Arkani-Hamed, (2012). Impact-induced mantle dynamics on Mars, Icarus
923 218, 278–289.
924 Roberts, J.H., and J. Arkani-Hamed (2017). Effects of Basin-Forming Impacts on the Thermal
925 Evolution and Magnetic Field of Mars, Earth Palent. Sci. Letters, in press.
926 Roberts, J.H., Barnouin, O.S., (2012). The effect of the Caloris impact on the mantle dynamics
927 and volcanism of Mercury. J. Geophys. Res. (Planets) 117, E02007.
928 Ruedas, T., (2017). Globally smooth approximations for shock pressure decay in impacts, Icarus
929 289, 22–33.

930 Schmidt, R.M., Housen, K.R., (1987). Some recent advances in the scaling of impact an
931 explosion cratering. Int. J. Impact Eng. 5, 543–560.
932 Senshu, H., K. Kuramoto, and T. Matsui, (2002). Thermal evolution of a growing Mars, J.
933 Geophys. Res., 107, E12, 5118, doi:10.1029/2001JE001819.
934 Shoemaker, E.M., (1962). Interpretation of Lunar Craters. Academic Press, San Diego, pp. 283–
935 359.
936 Solomatov, V.S., (2000). Fluid Dynamics of a Terrestrial Magma Ocean. In: Canup, R.M.,
937 Righter, K., 69 collaborating authors (Eds.), Origin of the earth and moon. University of Arizona
938 Press, Tucson, pp. 323–338.
939 Thompson, S., Lauson, H., (1972). Improvements in the CHART D Radiation- Hydrodynamic
940 Code III: Revised Analytic Equations of State. Sandia National Laboratory Report SC-RR-71
941 0714. 113 p.
942 Thompson, S.L., (1990). ANEOS analytic equations of state for shock physics codes input
943 manual. Sandia National Laboratories report SAND89-2951.
944 Tonks, W.B., and H.J. Melosh, (1992). Core Formation by Giant Impacts, Icarus 100, 326-346.
945 Tonks, W.B., and H.J. Melosh, (1993). Magma Ocean Formation Due to Giant Impacts, J.
946 Geophys. Res., 98, 5319-5333.
947 Watters W.A., Zuber, M.T., Hager, B.H. (2009). Thermal perturbations caused by large impacts
948 and consequences for mantle convection, J. Geophys. Res., 114, E02001.
949 Wünnemann, K., Collins, G.S., Melosh, H.J., (2006). A strain-based porosity model for use in
950 hydrocode simulations of impacts and implications for transient-crater growth in porous targets.
951 Icarus 180, 514–552.
952 Wünnemann K, Collins GS, Osinski, GR. (2008). Numerical modelling of impact melt
953 production in porous rocks. Earth and Planetary Science Letters, 269(3-4), 530-539.
954

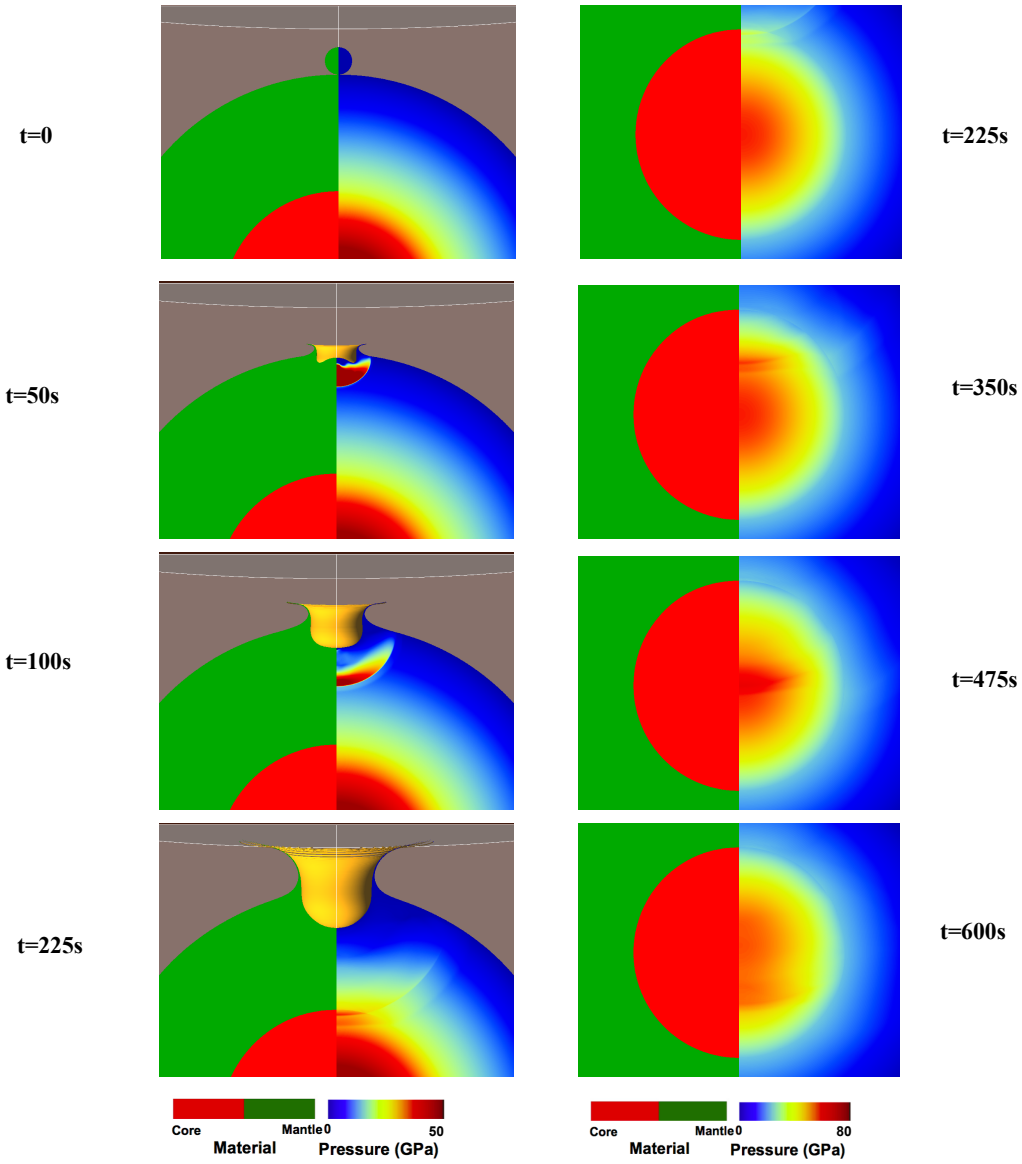

Figure 1: Time evolution of the total pressure (shock + lithostatic) inside a differentiated Mars size body during the first 600 seconds after the impact, caused by a 200 km radius undifferentiated impactor at 10 km/s impact velocity. In our models, the Martian core is liquid. The lithostatic pressure is adopted from Monteux and Arkani-Hamed [2016] and the pre-impact temperature profile is illustrated in Figure 4 (cold profile). The four left panels represent 4 specific times (from top to bottom): t=0s, t=50s, t=100s and t=225s with a focus on the impacted mantle. The four right panels represent 4 times (from top to bottom): t=225s, t=350s, t=475s and t=600s with a focus on the impacted core. Note the change in the pressure scales between the left and right panels.

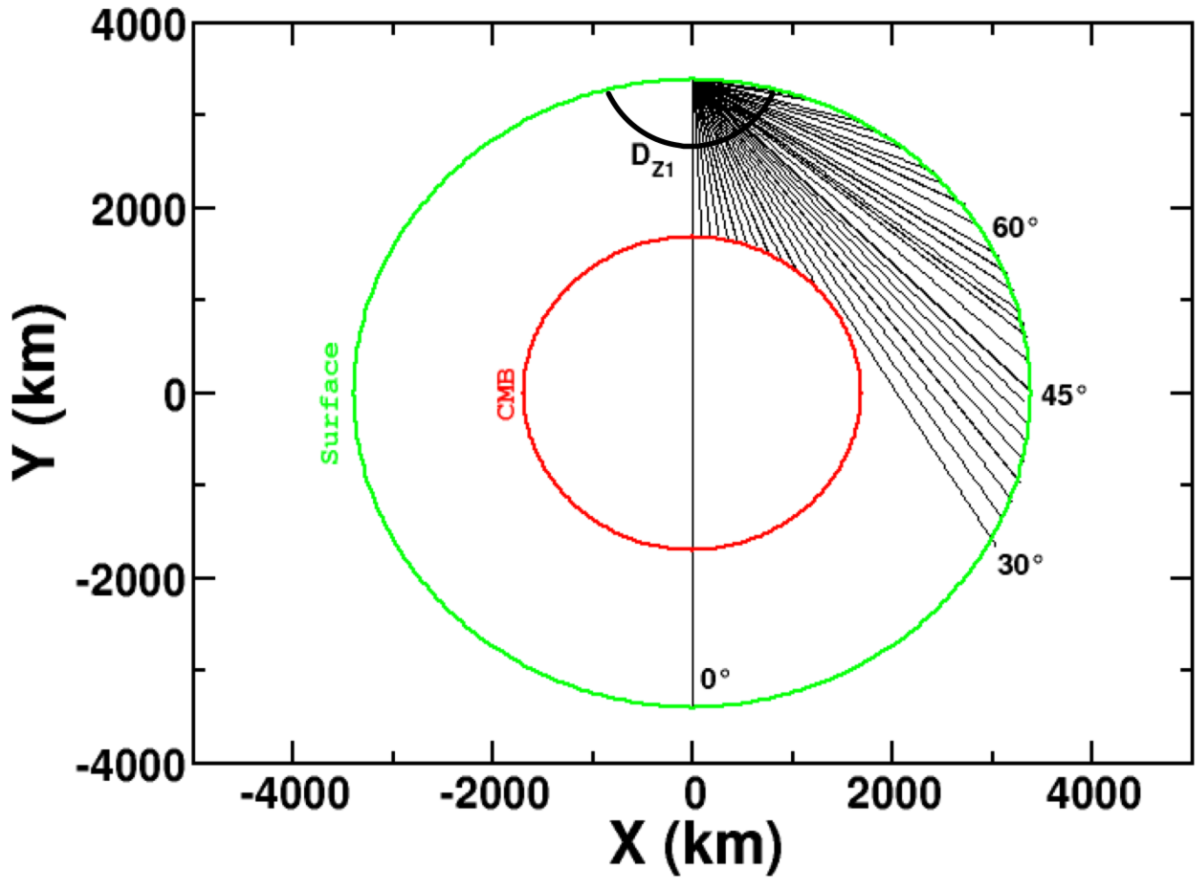

Figure 2: The rays along which the shock pressure is monitored. The different rays illustrated here with thin solid lines correspond to different values of β ranging between 0° (vertical) and 80°. The black thick line at D_{Z1} represents the boundary between zones 1 and 2 (in this figure, the boundary is placed arbitrarily). Between the impact site and D_{Z1}, the pressure decreases exponentially while beyond D_{Z1}, the pressure decrease follows a power law (see section 2.3). The numbers 30, 45, and 60 show the β values in degrees.

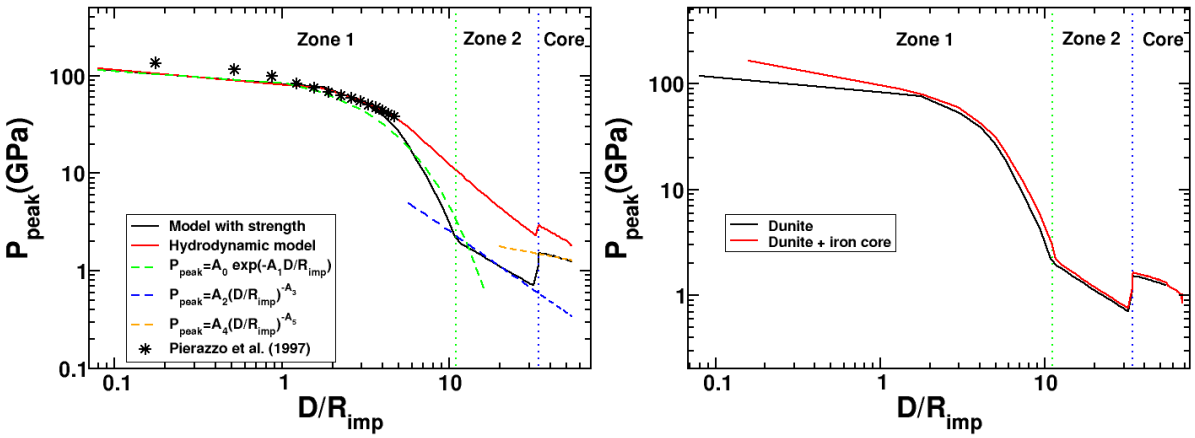

974

975 **Figure 3: Left: Shock pressure along the axis of symmetry (β=0°) as a function of the**
976 **distance from the impact site. In this (reference) case, R_{imp}=50km and V_{imp}=10km/s. The**
977 **green, blue and orange dashed lines represent the fits obtained using Eq. 1a, 1b and 1c**
978 **respectively. Black stars represent the results from Pierazzo et al., [1997] for V_{imp}=10km/s**
979 **and R_{imp} ranging between 0.4 and 10km. Right: Same case as left panel (Model with**
980 **strength) considering a dunitic (black solid line) impactor and a differentiated impactor**
981 **with a 24 km core radius (red solid line).**

982

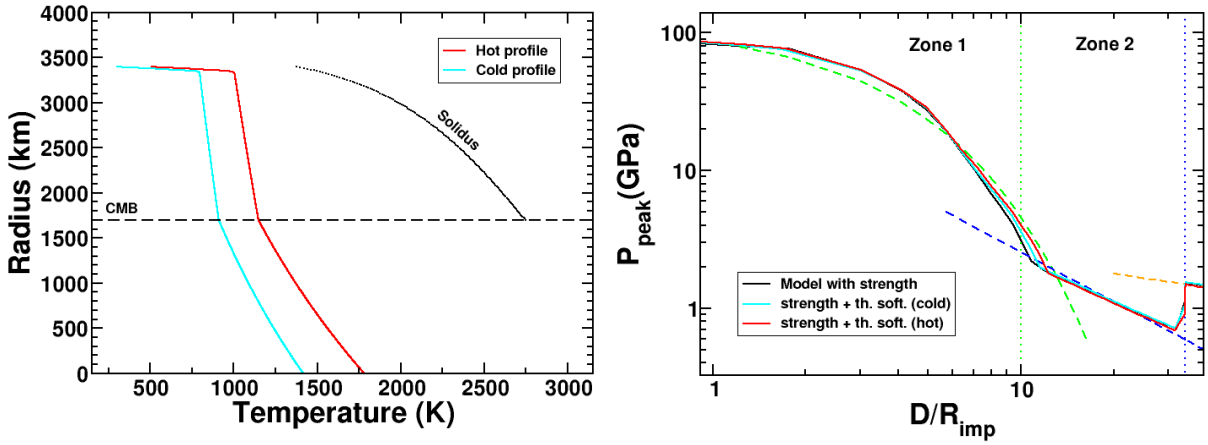

Figure 4: Left: Pre-impact temperature profiles and solidus used for models including thermal softening. The cyan line represents the "cold" profile with a pre-impact surface temperature of 273K while the red line represents the "hot" profile with a pre-impact surface temperature of 500K. Right: Shock pressure along the axis of symmetry (β=0°) as a function of the distance from the impact site. The black line represents the reference case (same as Figure 3 for model with strength, R_{imp}=50km and V_{imp}=10km/s). The cyan and red lines represent the shock pressure decay for the models accounting for thermal softening considering the "cold" and the "hot" pre-impact temperature profile respectively illustrated on the left figure. The green, blue and orange dashed lines represent the fits obtained using Eq. 1a, 1b and 1c respectively.

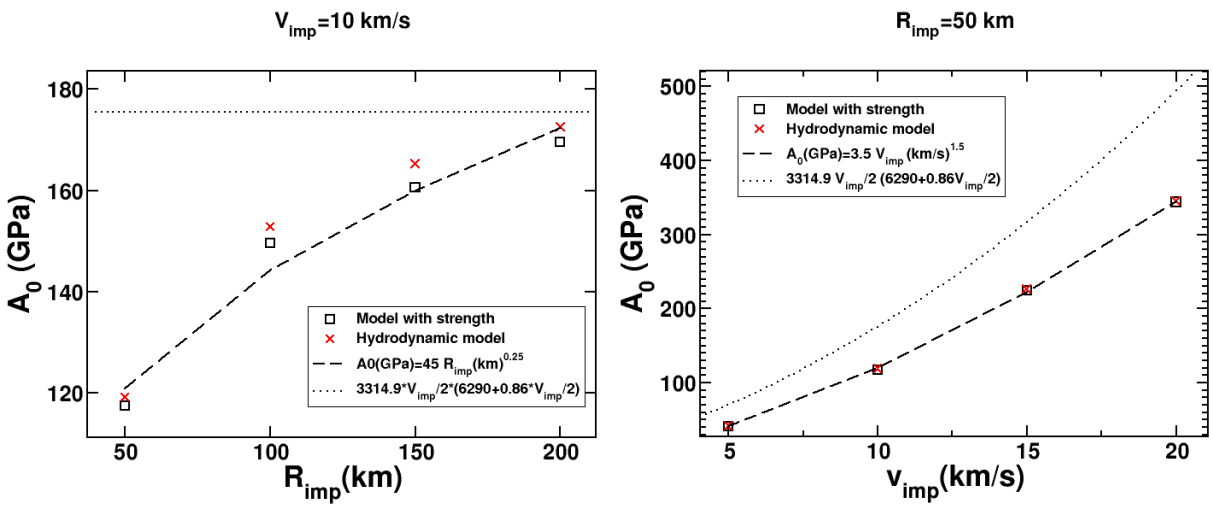

Figure 5: The maximum peak shock pressure A_0 (Eq. 1a) as a function of the impactor radius R_{imp} (left), and the impact velocity V_{imp} (right). The dotted lines represent the result from the planar impact approximation [Melosh, 1989] considering that both the impactor and the target are made of dunite (with ρ_0=3314.9, C_0=6290 m/s and S=0.86 for both iSALE models and planar impact approximation).

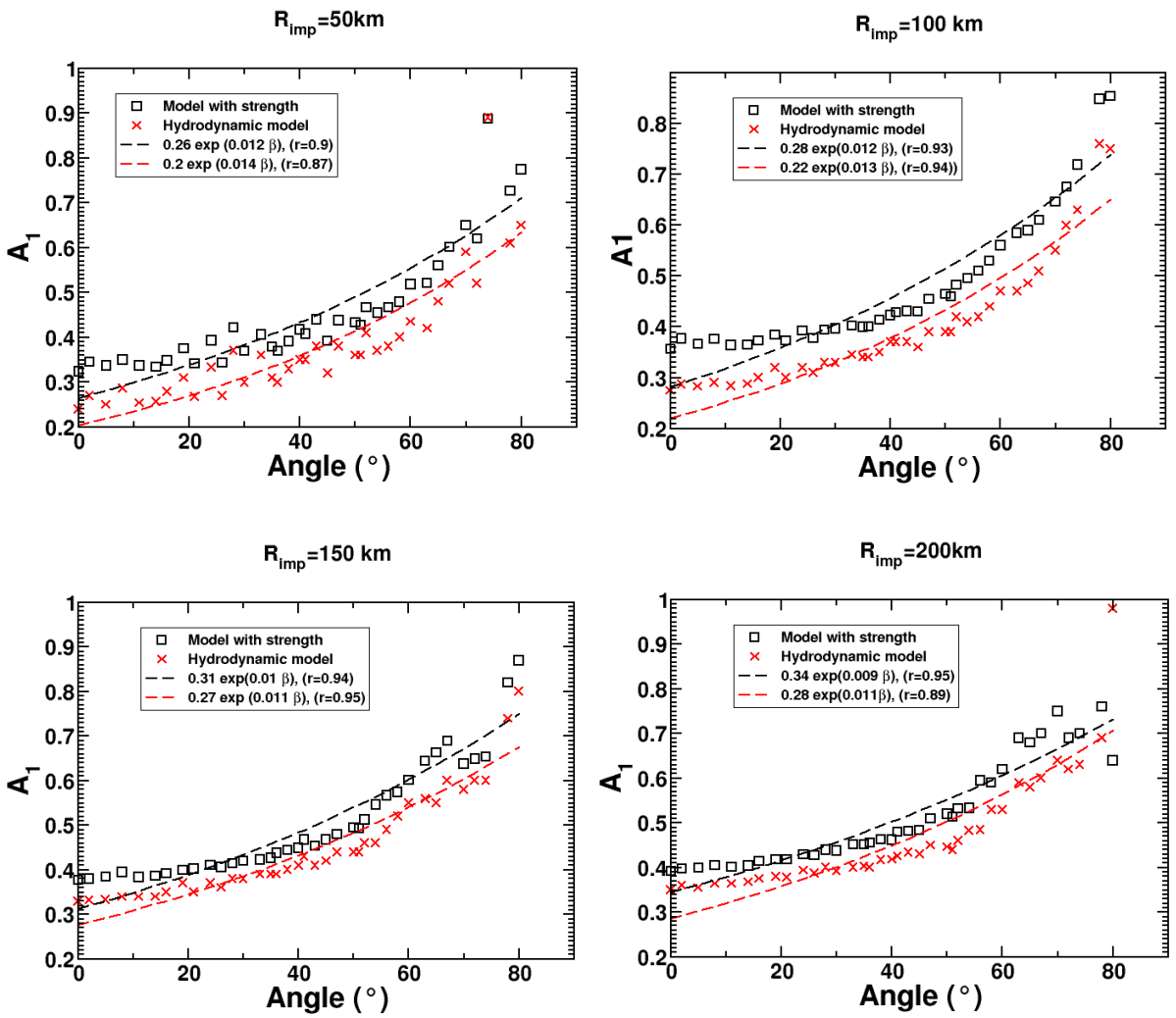

Figure 6a: A_1 **as a function of the ray angle** β **(Eq. 1a:** $P_{Z1}=A_0\ exp(-A_1\ D/R_{imp})$**) for different impactor radii, but the same impact velocity (**V_{imp}**=10km/s).** A_1 **values are obtained by fitting the peak shock pressure in Zone 1 (close to the impact site) from iSALE models. The correlation coefficient (*r*), between the values obtained by the iSALE model and by the scaling law is mentioned in the legend box.**

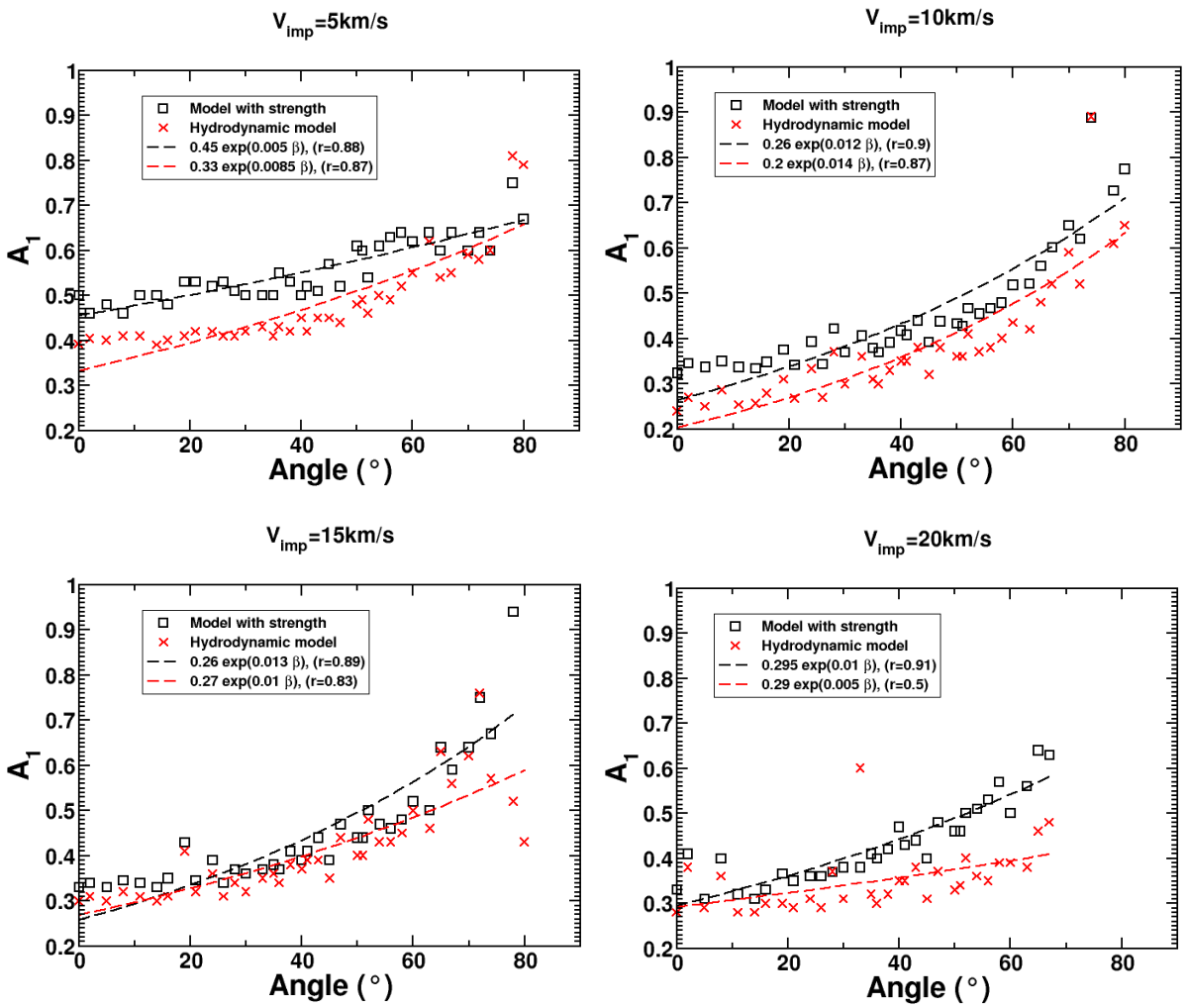

Figure 6b: A_1 **as a function of the ray angle** β **(Eq. 1a:** $P_{Z1}=A_0\ exp(-A_1\ D/R_{imp})$**) for different impact velocities (**R_{imp}**=50km).** A_1 **values are obtained by fitting the peak shock pressure in Zone 1 (close to the impact site) from iSALE models. The correlation coefficients (*r*), between the values obtained by the iSALE model and by the scaling law is mentioned in the legend box.**

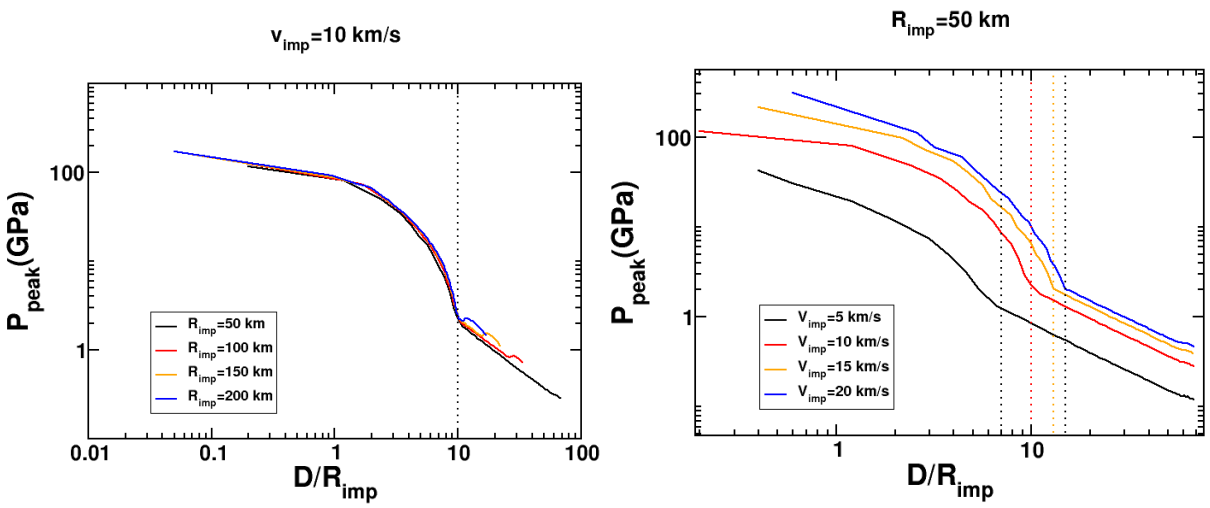

Figure 7: Shock pressure along the ray angle β=36° as a function of the distance from the impact site for different impactor sizes with an impact velocity of 10 km/s (left) and different impact velocities for an impactor radius of 50 km (right). On the left panel, the vertical dotted line represents $D_{Z1}=10\ R_{imp}$. On the right panel, the four vertical dotted lines represent different values of D_{Z1} corresponding to the different values of V_{imp}.

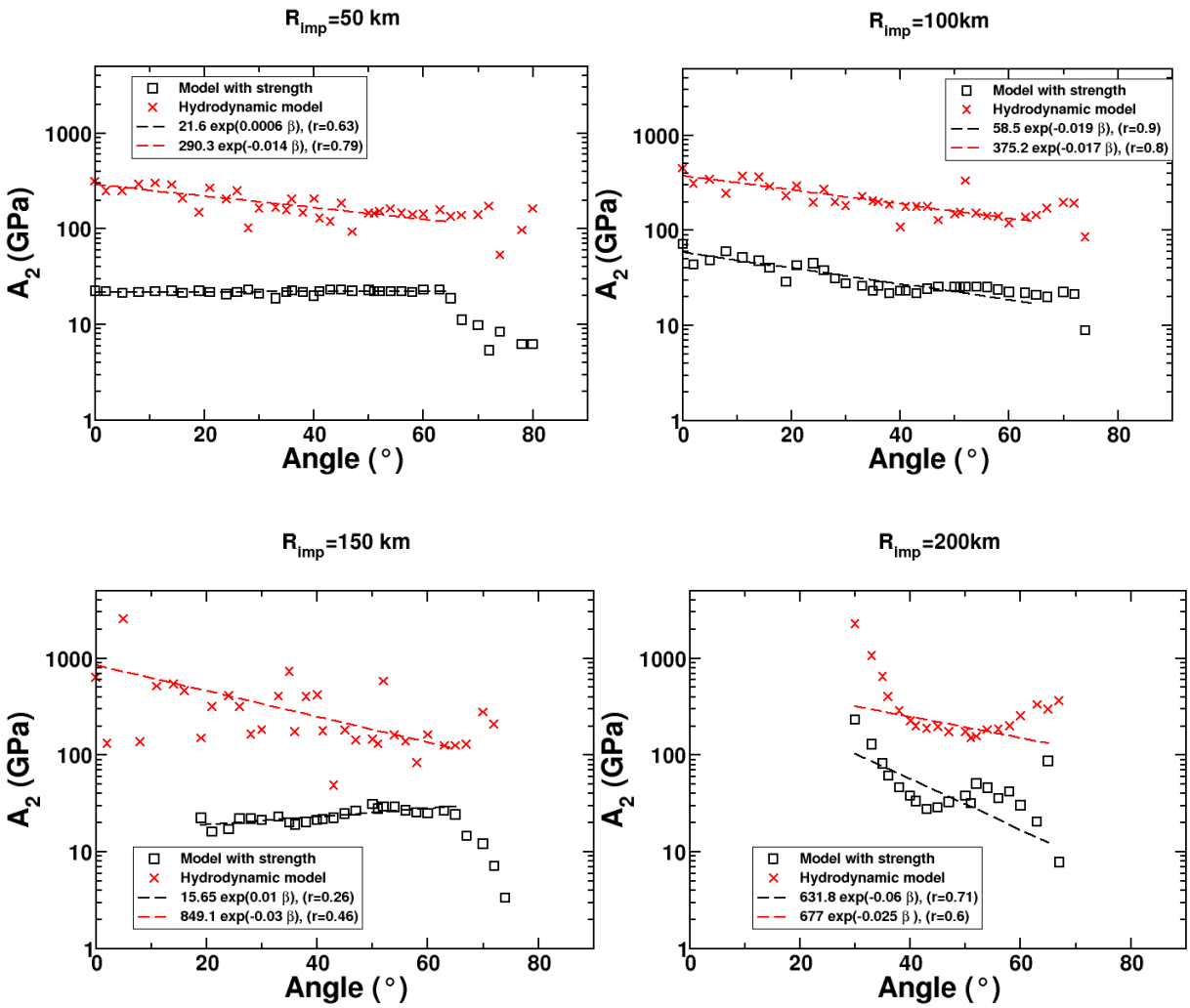

Figure 8a: A_2 **as a function of the ray angle** β **(Eq. 1b:** $P_{Z2}=A_2\ (D/R_{imp})^{-A_3}$**) for different impactor radii, but an impact velocity of 10 km/s.** A_2 **values are obtained by fitting the shock pressure in Zone 2 (beyond** D_{Z1}**) from iSALE models. In these figures,** D_{Z1}**=10. The correlation coefficient (***r***) for each scaling law is mentioned in the legend box (note that fits are restricted to** $\beta \leq 65°$**).**

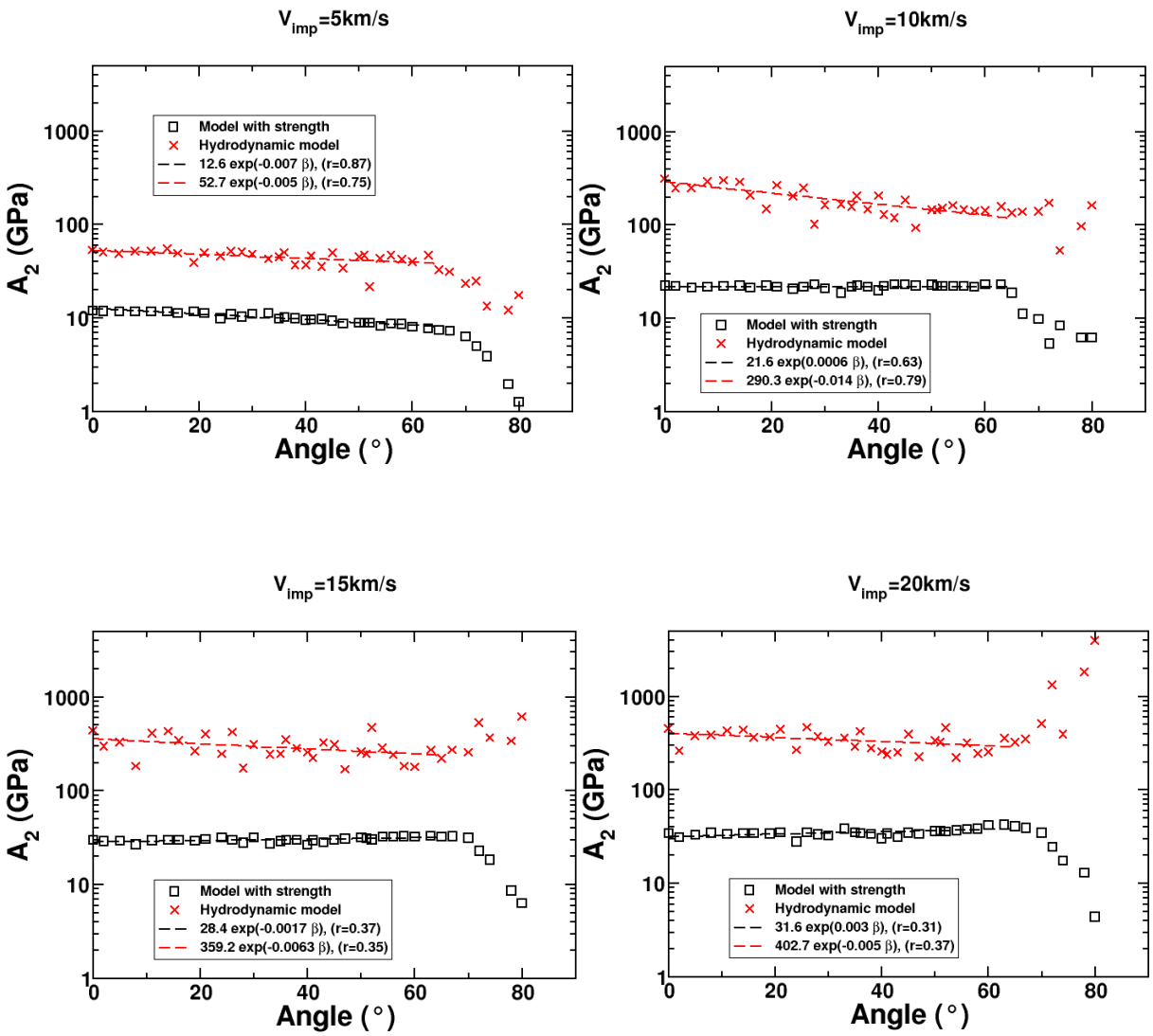

Figure 8b: A_2 **as a function of the ray angle** β **(Eq. 1b:** $P_{Z2}=A_2\,(D/R_{imp})^{-A_3}$**) for different impact velocities, but an impactor radius of 50 km.** A_2 **values are obtained by fitting the shock pressure in Zone 2 (beyond** D_{Z1}**) from iSALE models. In these figures,** D_{Z1} **= 7, 10, 13 and 15 for** V_{imp} **= 5, 10, 15 and 20 km/s respectively. The correlation coefficient (***r***) for each scaling law is mentioned in the legend box (note that fits are restricted to** $\beta \leq 65°$**).**

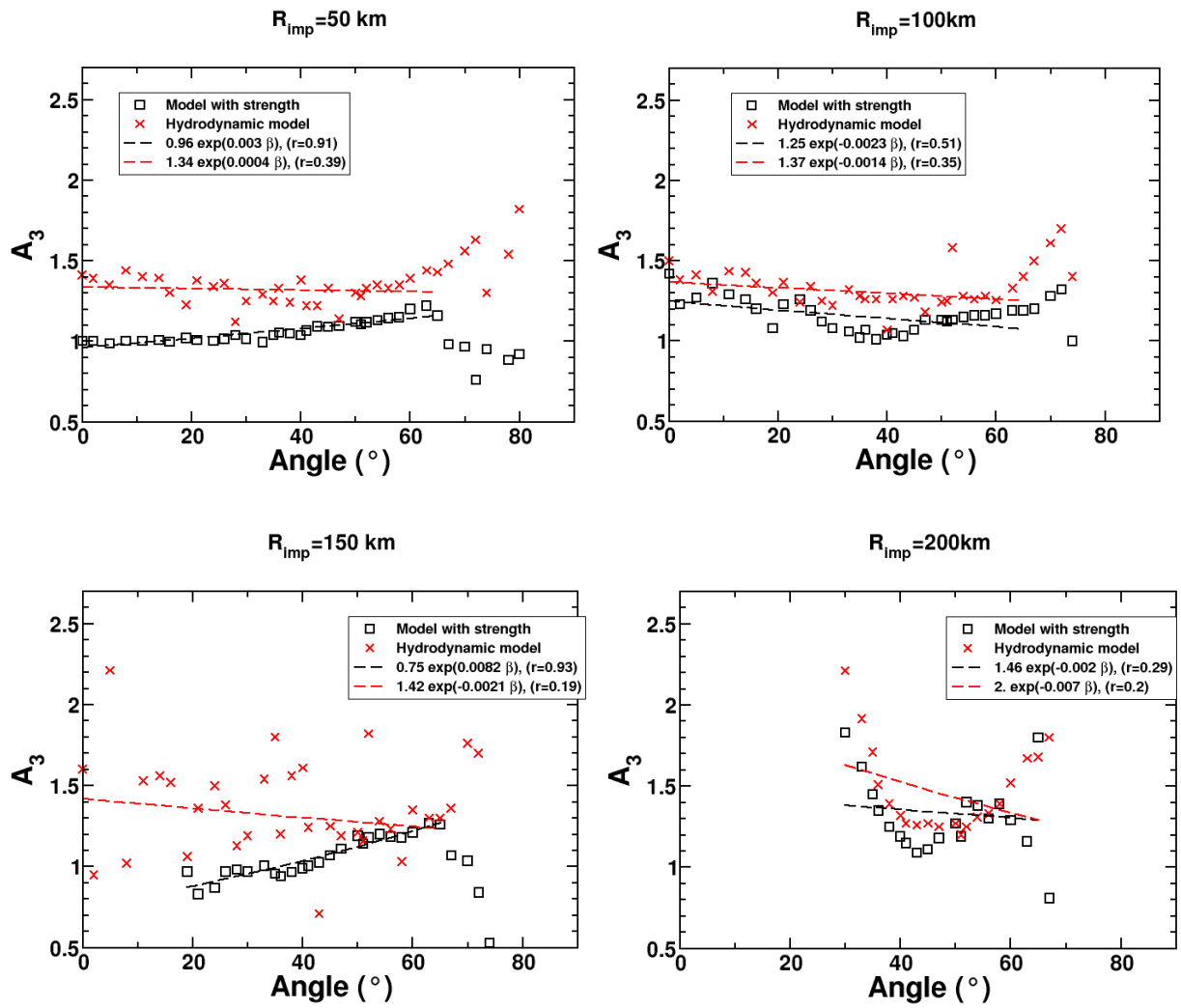

Figure 9a: A_3 as a function of the ray angle β (Eq. 1b: $P_{Z2}=A_2\ (D/R_{imp})^{-A_3}$) for different impactor radii. A_3 values are obtained by fitting the shock pressure in Zone 2 (beyond D_{Z1}) from iSALE models. In these figures, D_{Z1}=10. The correlation coefficient (r) for each scaling law is mentioned in the legend box (note that fits are restricted to $\beta \leq 65°$).

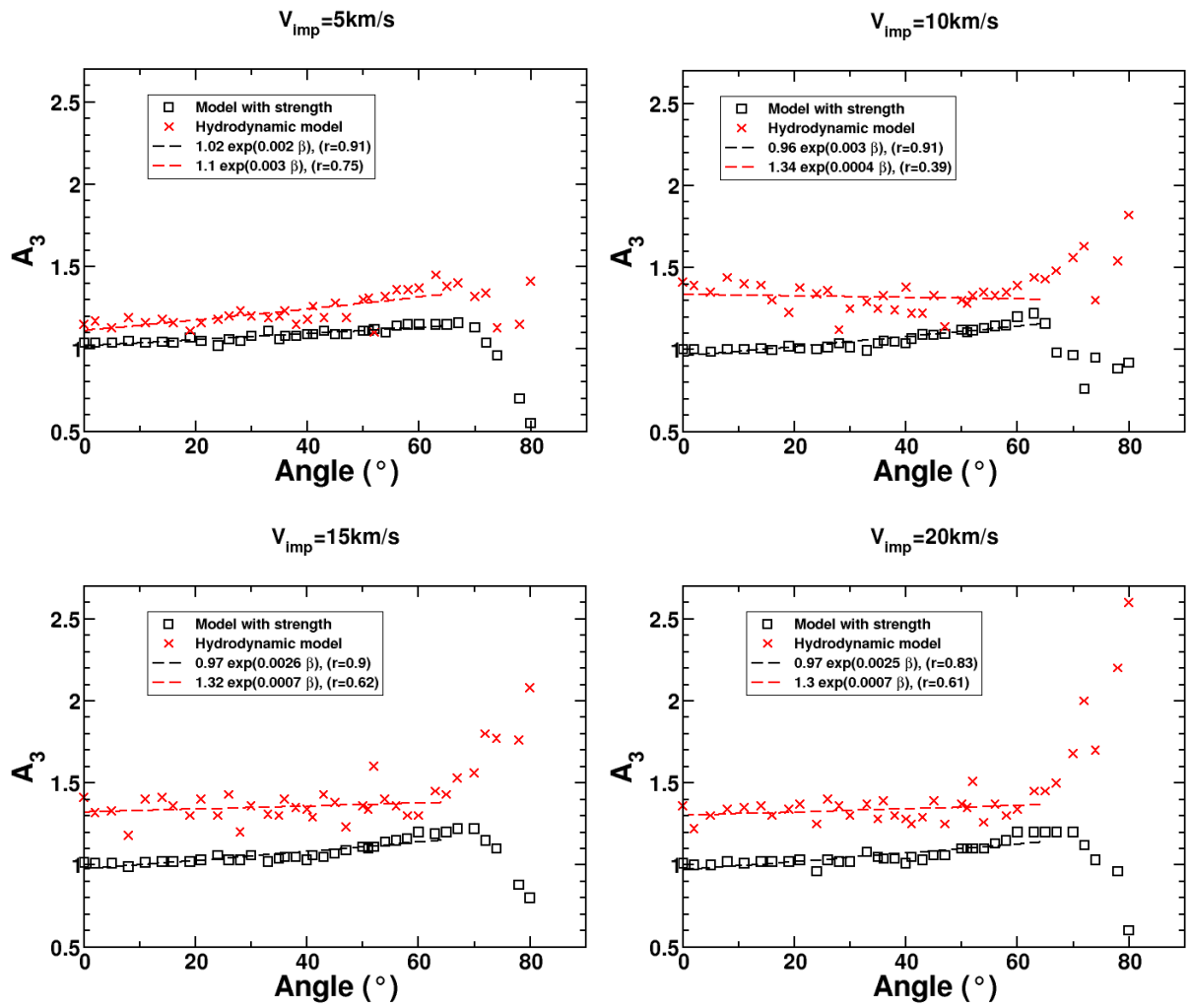

Figure 9b: A_3 **as a function of the ray angle** β **(Eq. 1b:** $P_{Z2}=A_2\ (D/R_{imp})^{-A_3}$**) for different impact velocities.** A_3 **values are obtained by fitting the shock pressure in Zone 2 (beyond** D_{Z1}**) from iSALE models. In these figures,** D_{Z1}**=7, 10, 13 and 15 for** V_{imp}**=5, 10, 15 and 20 km/s respectively. The correlation coefficient (***r***) for each scaling law is mentioned in the legend box (note that fits are restricted to** $\beta \leq 65°$**).**

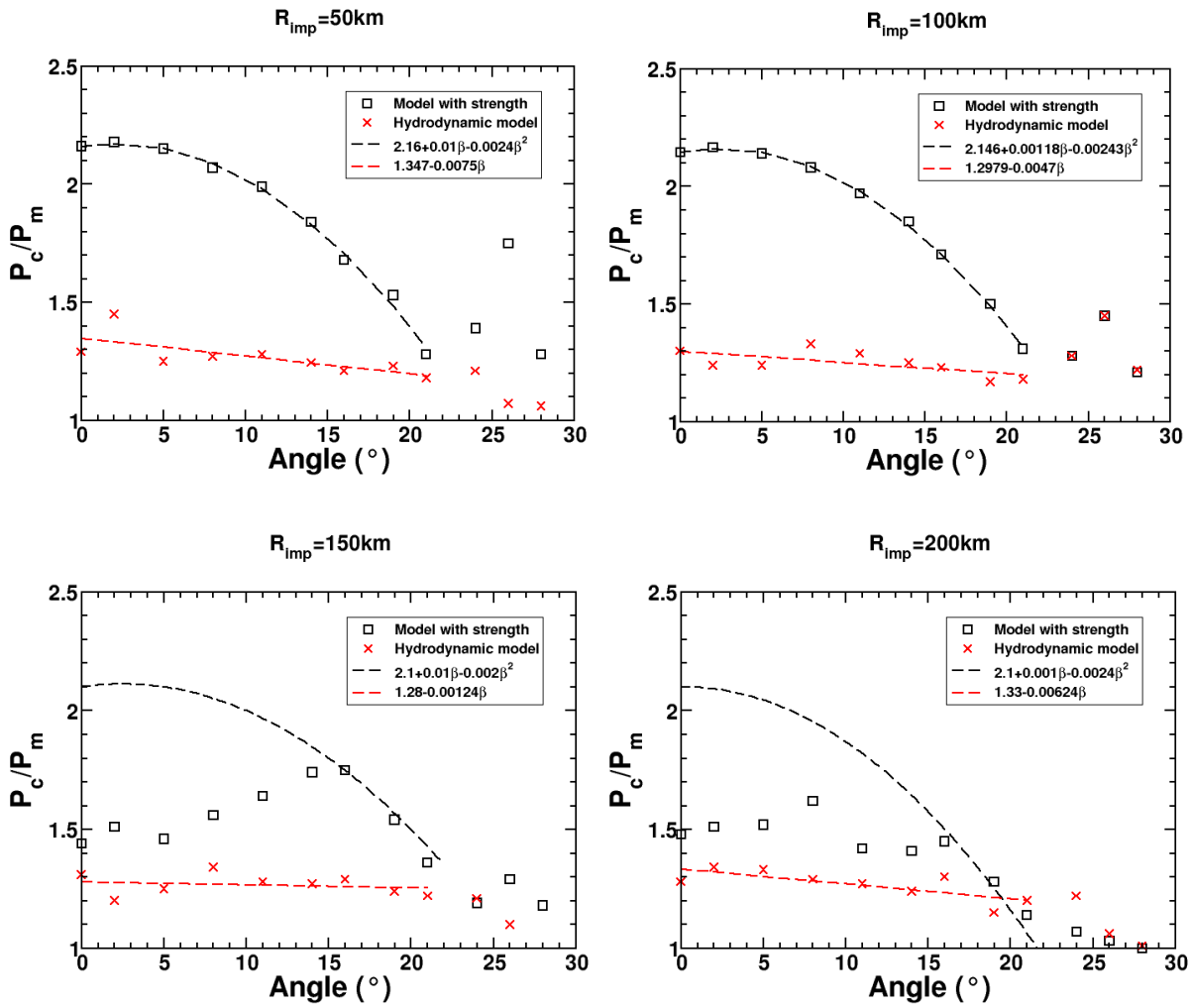

Figure 10a: Shock pressure jump P_c/P_m at the core mantle boundary as a function of the ray angle β for different impactor sizes, but a single impact velocity of 10 km/s. Data obtained from iSale models are shown with symbols while the analytical expression from Eq. 1c is illustrated with dashed lines. For values of β larger than 30°, the rays do not cross the CMB.

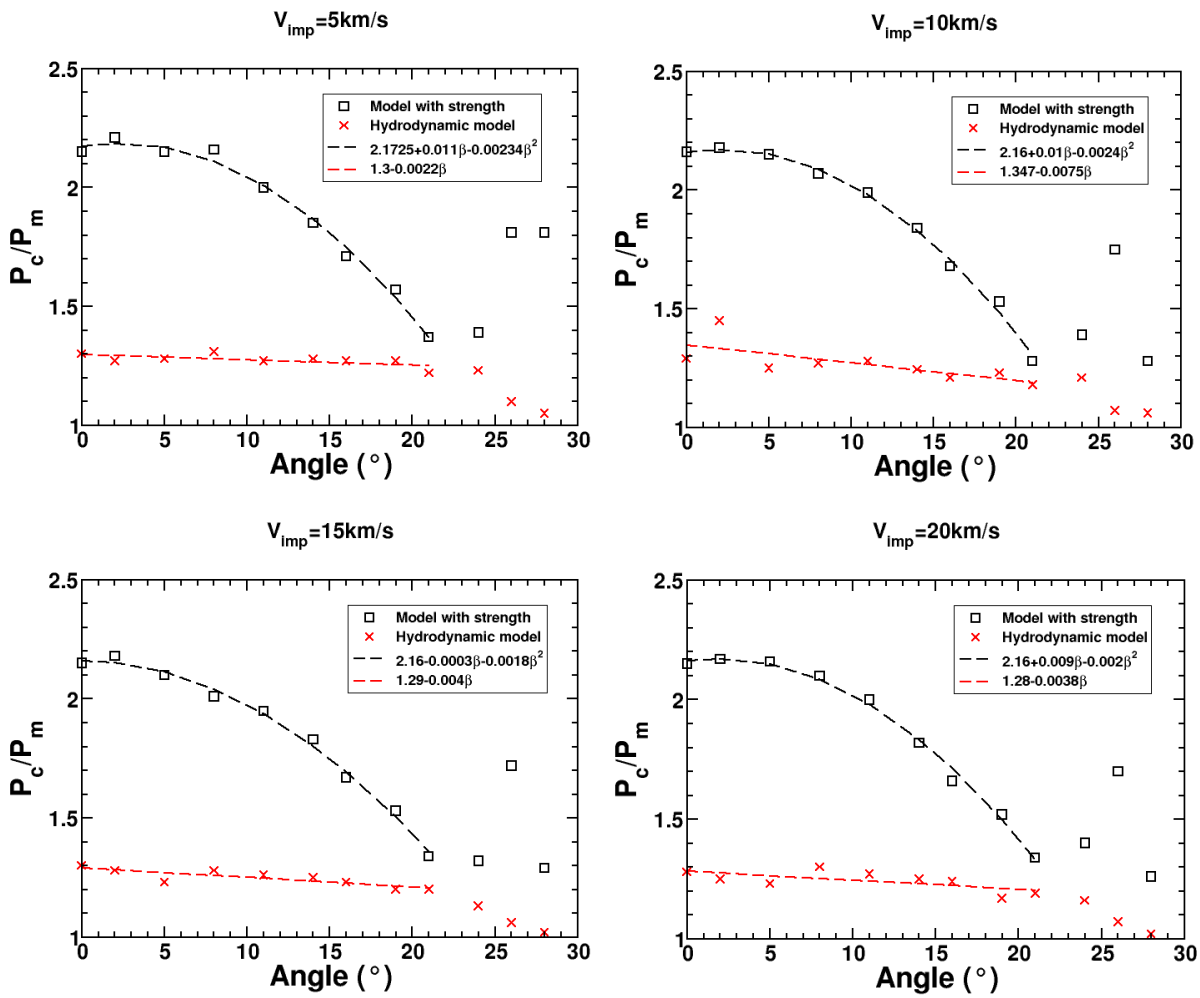

Figure 10b: Shock pressure jump P_c/P_m at the core mantle boundary as a function of the ray angle β for different impact velocities, but a single impactor radius of 50 km. Data obtained from iSale models are shown with symbols while the analytical expression from Eq. 1c is illustrated with dashed lines. For values of β larger than 30°, the rays do not cross the CMB.

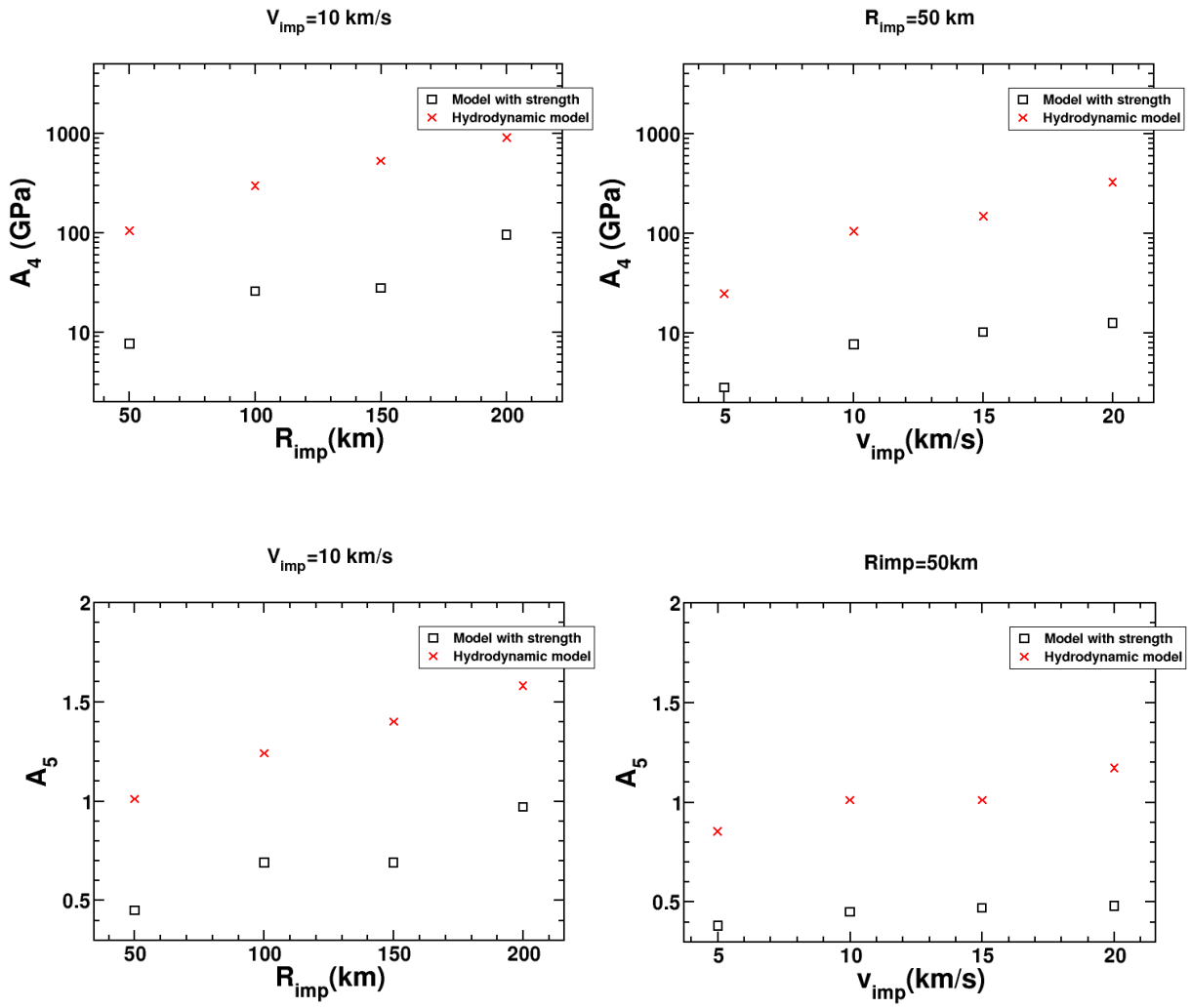

Figure 11: A_4 **and** A_5 **values (Eq. 1c:** $P_{core}= A_4\ (D/R_{imp})^{-A_5}$**) as functions of the impactor radius (left panels) and impact velocity (right panels).**

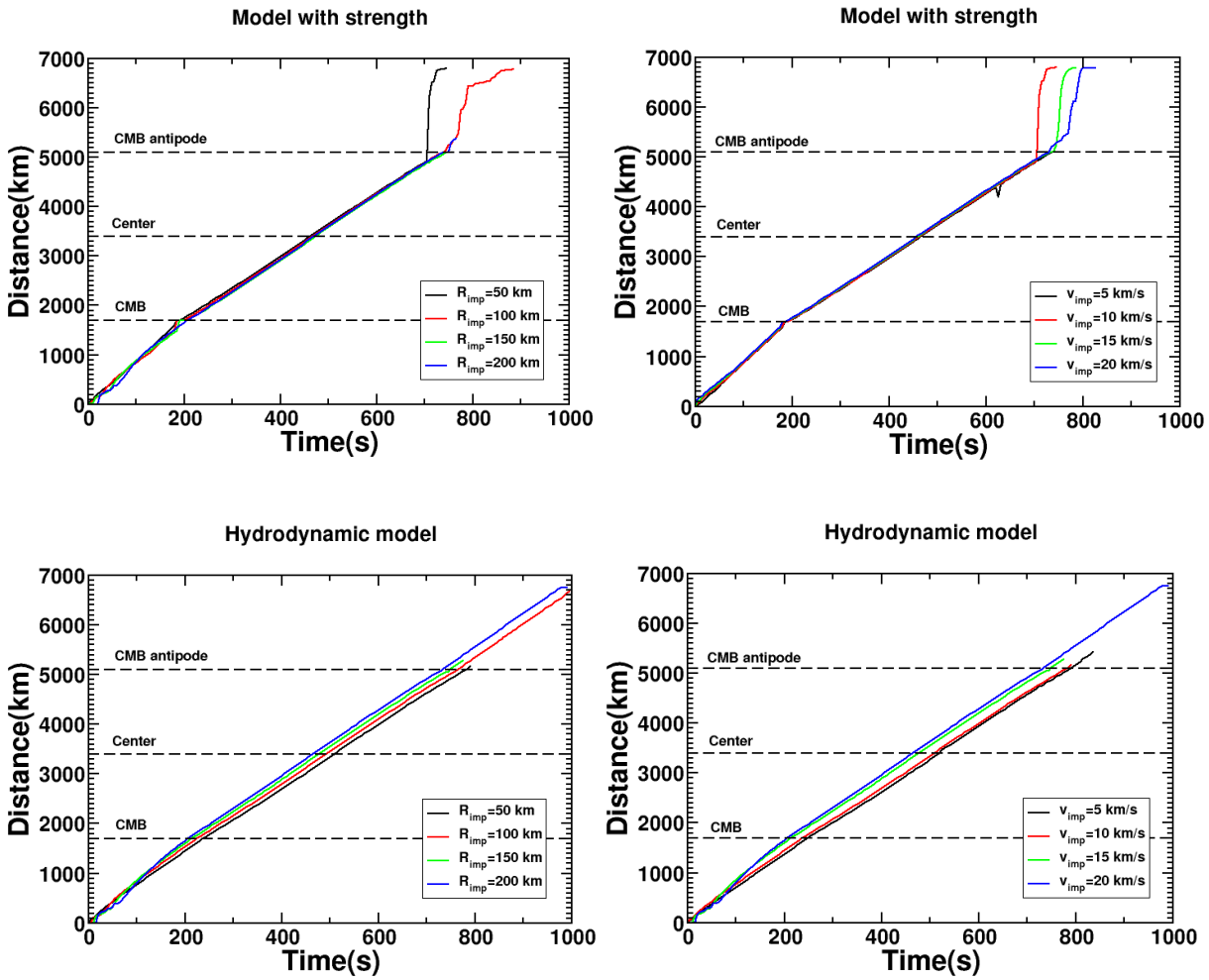

Figure 12: Position of the peak shock pressure as a function of the time after the impact for the models with strength (top panels) and the hydrodynamic models (bottom panels).

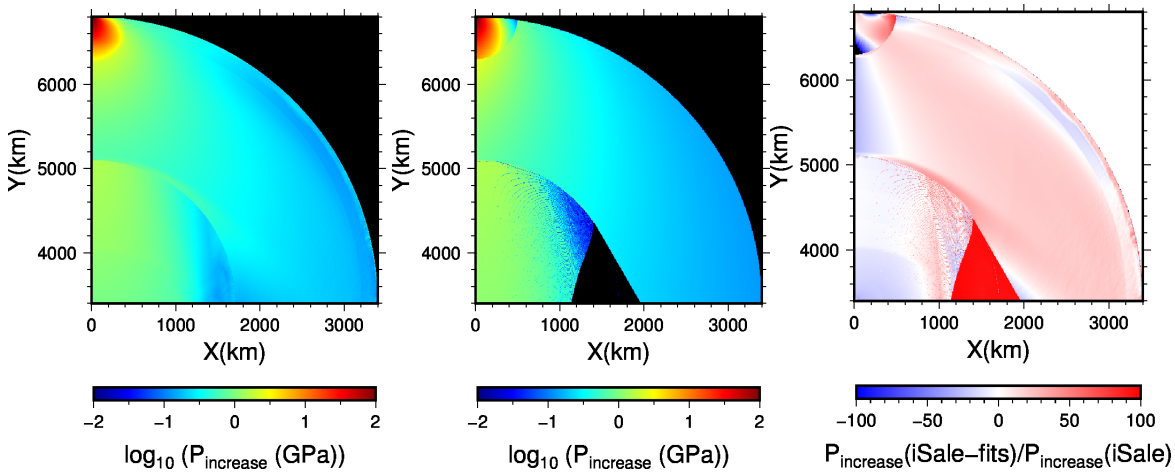

(a)

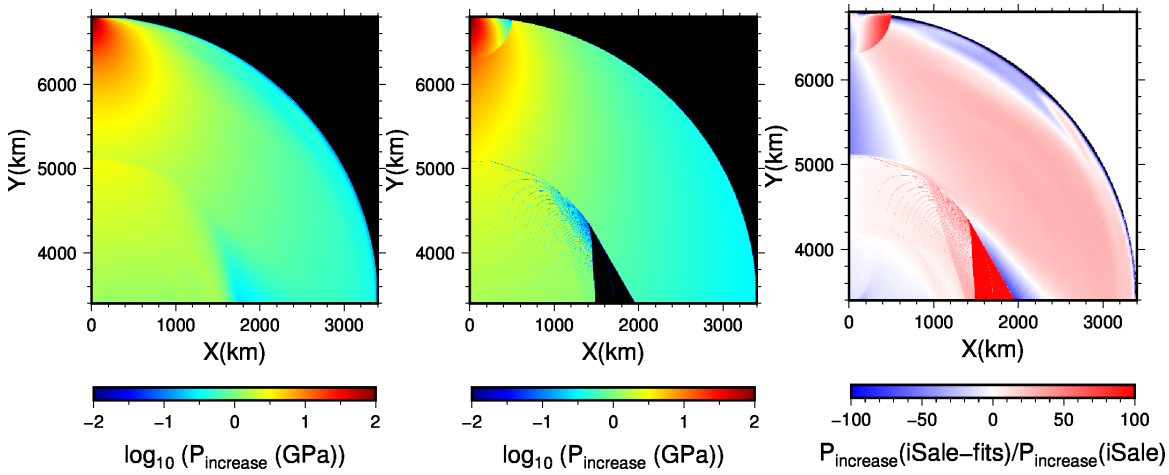

(b)

Figure 13: Comparison of the maximum shock pressure experienced after an impact within a differentiated Mars size planet with R_{imp}=50 km and V_{imp}=10 km/s. (a) is for model with strength and (b) is for Hydrodynamic model. The left panel represents the result from the iSALE model and the middle panel represents the model obtained from our scaling laws (Eqs. 1a, 1b and 1c). The right panel shows the error relative to the iSALE model (in %). Note that only the impacted hemisphere is shown in this figure, because the scaling laws are derived for this hemisphere.

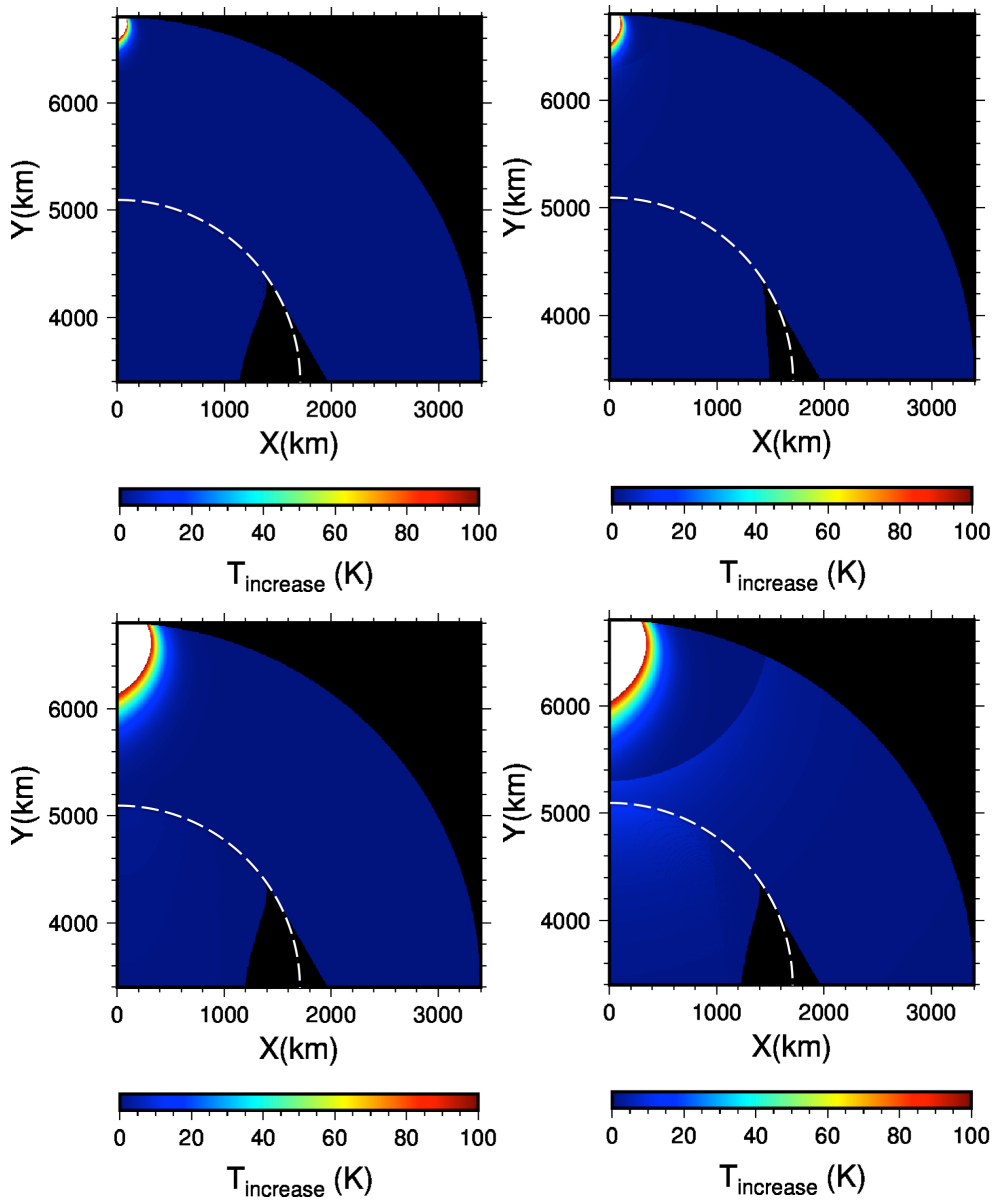

Figure 14: Temperature increase after an impact within a differentiated Mars size planet. The first line: R_{imp}=50 km and V_{imp}=10 km/s, and the second line: R_{imp}=150 km and V_{imp}=10 km/s (Left: Model with strength, Right: Hydrodynamic model). All panels represents the model obtained from our scaling laws (Eqs. 1a, 1b and 1c) combined with the impact induced temperature increase model (Eqs. 4, 5 and 6) from Watters et al., (2009) (with C=7.24km/s, S=1.25, $\rho=\rho_m$ for the mantle and C=4km/s, S=1.6, $\rho=\rho_c$ for the core [Arkani-Hamed and Olson, 2010]). The white dashed line represents the CMB.

Table 1: Typical physical parameter values for numerical hydrocode models.

Target radius	R	3400 km (Rivoldini et al., 2011)
Target core radius	R_{core}	1700 km (Rivoldini et al., 2011)
Impactor radius	R_{imp}	50-200 km
Impact velocity	V_{imp}	5-20 km/s
Mantle properties (Dunite) :		(Benz et al., 1989)
		Model with strength
Initial density	ρ_m	3314 kg/m^3
Heat capacity	c_p	1200 J/kg/m^3
Equation of state type		ANEOS for dunite (also stands for hydrodynamic models)
Poisson ratio		0.25
Strength Model		Rock
(iSALE parameters)		(Y_{i0}=10 MPa, μ_i=1.2,Y_{im}=3.5 GPa)
Acoustic Fluidization Model		Block
(iSALE parameters)		(t_{off}=16 s, c_{vib}=0.1 m/s, vib_{max}=200 m/s)
Damage Model		[Ivanov et al., 1997]
(iSALE parameters)		(ε_{fb}=10^{-4}, B=10^{-11}, P_c=3x10^8 Pa)
Thermal softening model		[Ohnaka, 1995]
(iSALE parameters)	ξ	1.2
	T_m	1375 K [Davison, 2010]
Low density weakening and porosity models		None
*Core properties (**Iron**):*		(Thomson, 1990)
		All models
Initial density	ρ_c	7840 kg/m^3
Heat capacity	c_p	800 J/kg/m^3
Equation of state type		ANEOS for iron
Damage, low density weakening thermal softening and porosity models		None

1111
1112

1113 **Table 2: Typical numerical parameter values for numerical hydrocode models.**

Horizontal cells	2000
Vertical cells	4000
Grid spacing	2 km
Cells per projectile radius (CPPR) :	
Impactor :	25 *(for R_{imp}=50km)* to 100 *(for R_{imp}=200km)*
Target Mantle	1700
Target Core	850
Maximum time step (dt_{max})	0.05s

1114

Table 3: Values of b_1, b_2, b_3, b_4 and b_5 obtained by fitting the results from the numerical models (Figures 10a and 10b) with Eqs. 2a and b. The values for models with strength are separated from those of hydrodynamic models with no strength and are shown as a function of R_{imp} and V_{imp}.

Models with strength	*b1*	*b2*	*b3*
R_{imp}=50km (V_{imp}=10km/s)	2.16	$1.x10^{-2}$	$-2.4\ x10^{-3}$
R_{imp}=100km (V_{imp}=10km/s)	2.15	$1.2x10^{-3}$	$-2.4\ x10^{-3}$
R_{imp}=150km (V_{imp}=10km/s)	2.1	$1.x10^{-2}$	$-2.\ x10^{-3}$
R_{imp}=200km (V_{imp}=10km/s)	2.1	$1.x10^{-3}$	$-2.4\ x10^{-3}$
V_{imp}=5 km/s (R_{imp}=50km)	2.17	$1.1x10^{-2}$	$-2.3\ x10^{-3}$
V_{imp}=10 km/s (R_{imp}=50km)	2.16	$1.x10^{-2}$	$-2.4\ x10^{-3}$
V_{imp}=15 km/s (R_{imp}=50km)	2.16	$3.x10^{-4}$	$-1.8\ x10^{-3}$
V_{imp}=20 km/s (R_{imp}=50km)	2.16	$9.x10^{-3}$	$-2.\ x10^{-3}$
Hydrodynamic models	*b4*	*b5*	
R_{imp}=50km (V_{imp}=10km/s)	1.35	$-7.5\ x10^{-2}$	-
R_{imp}=100km (V_{imp}=10km/s)	1.3	$-4.7\ x10^{-3}$	-
R_{imp}=150km (V_{imp}=10km/s)	1.28	$-1.2\ x10^{-3}$	-
R_{imp}=200km (V_{imp}=10km/s)	1.33	$-6.2\ x10^{-3}$	-
V_{imp}=5 km/s (R_{imp}=50km)	1.3	$-2.2\ x10^{-4}$	-
V_{imp}=10 km/s (R_{imp}=50km)	1.35	$-7.5\ x10^{-2}$	-
V_{imp}=15 km/s (R_{imp}=50km)	1.29	$-4.\ x10^{-3}$	-
V_{imp}=20 km/s (R_{imp}=50km)	1.28	$-3.8\ x10^{-3}$	-

Table 4: Velocity of the peak shock pressure propagation in the mantle and in the core for the models with strength and hydrodynamic models, obtained fitting the results from Figure 12 with a linear expression.

	Target mantle	Target core
Models with strength		
R_{imp}=50km (V_{imp}=10km/s)	8.84 km/s	6.38 km/s
R_{imp}=100km (V_{imp}=10km/s)	8.52 km/s	6.44 km/s
R_{imp}=150km (V_{imp}=10km/s)	8.58 km/s	6.47 km/s
R_{imp}=200km (V_{imp}=10km/s)	8.93 km/s	6.50 km/s
V_{imp}=5 km/s (R_{imp}=50km)	9.04 km/s	6.33 km/s
V_{imp}=10 km/s (R_{imp}=50km)	8.84 km/s	6.38 km/s
V_{imp}=15 km/s (R_{imp}=50km)	8.80 km/s	6.36 km/s
V_{imp}=20 km/s (R_{imp}=50km)	8.60 km/s	6.38 km/s
Hydrodynamic models		
R_{imp}=50km (V_{imp}=10km/s)	6.96 km/s	6.36 km/s
R_{imp}=100km (V_{imp}=10km/s)	7.60 km/s	6.40 km/s
R_{imp}=150km (V_{imp}=10km/s)	8.33 km/s	6.46 km/s
R_{imp}=200km (V_{imp}=10km/s)	8.77 km/s	6.53 km/s
V_{imp}=5 km/s (R_{imp}=50km)	6.76 km/s	6.41 km/s
V_{imp}=10 km/s (R_{imp}=50km)	6.96 km/s	6.36 km/s
V_{imp}=15 km/s (R_{imp}=50km)	8.33 km/s	6.46 km/s
V_{imp}=20 km/s (R_{imp}=50km)	8.79 km/s	6.53 km/s